POLITECNICO DI TORINO

Master's Degree in Aerospace Engineering

Master's Degree Thesis

Numerical model of an Air-Turbo-Rocket engine for a hypersonic Mach 5 passenger aircraft

Supervisors

Prof. Michele FERLAUTO

Dr. Bayindir Huseyin SARACOGLU

Eng. Karel VAN DEN BORRE

Candidate

Federico PETTINATO

Accademic Year 2023/2024

Abstract

In the context of hypersonic propulsion for civil purposes and a more sustainable aeronautic industry, the air-turbo-rocket expander engine (ATR-EXP) has been studied through a transient lumped model. To fulfill the trajectory mission of the EC-funded MORELESS project, based on previous works, three throttle variables have been identified. A sensitivity analysis has been conducted proving how and which combination of actuators can satisfy the control requests. The turbomachinery off-design behavior has been considered in simulating the ascend trajectory. A control strategy has been identified compliant within a subspace of throttle variables. The system stability has been demonstrated for a selection of critical steady-state conditions.

"Abbiamo due vite. La seconda inizia quando ci rendiamo conto di averne solo una."
Confucio

Acknowledgements

First of all I would like to thank the von Karman Institute community who, as the host institute, welcomed me warmly and provided me with all the necessary equipment and software.

I would like to thank Professor Ferlauto, supervisor of this thesis, who believed in my abilities from the first moment.

I would also like to thank Dr. Saracoglu for being my co-supervisor. Who guided me technically but also helped me grow professionally as an engineer.

I would also like to thank Eng. Karel Van den Borre for providing me constant guidance and precise advice in all the phases of this work.

Last, but certainly not least, I would like to thank my family and friends for their love and support.

Table of Contents

List of Tables

List of Figures

Introduction

Mach 5 Flight: Challenges and Advantages

The Air-Turbo-Rocket Expander engine, the subject of this thesis, is designed to contend with various flight regimes. Understanding these regimes is crucial to grasp the technical challenges involved. The Mach number, defined as the ratio between the fluid velocity and the speed of sound in the fluid, determines the flight regimes:

- **Subsonic**: Mach number less than 1. If Mach is below 0.3, compressibility effects are negligible.
- **Transonic**: Mach number between 0.8 and 1.3. Fluid moves at speeds comparable to sound.
- **Supersonic**: Mach number above 1. It is characterized by shock waves and sonic booms.
- **Hypersonic**: Mach number exceeds 5. High temperatures cause dissociation and the creation of partially ionized plasma. Therefore, structural design is heavily influenced by high thermal loads. Rounded shapes are preferred. In the LAPCAT and STRATOFLY projects, it is proposed that cryogenic fuel also be used as a structural coolant. Supersonic combustion chambers are needed.

Moreover, during a launch mission, a vehicle faces various atmospheric conditions and can experience trans-atmospheric flight. Initially, gas dynamics follow a continuous air model, transitioning to a rarefied air model at higher altitudes. Historically, multi-stage vehicles have been designed with a single type of propulsion system for each stage, optimizing for different altitude/Mach number regimes along the trajectory to increase overall system-specific impulse. For example, NASA's hypersonic aircraft demonstrators, the X-43 series, utilize subsonic aircraft propulsion for the first stage, followed by a Pegasus rocket for the second stage, with the scramjet-based research vehicle as the third stage. This configuration allows for autonomous flight from take-off to speeds greater than Mach 7 [11].

Figure 1: Illustration of Boeing X-43 [2].

Another critical aspect of propulsion is determining the altitude for nozzle matching, where exit pressure equals ambient pressure, optimizing net thrust. Below this altitude, the jet is overexpanded; above, it is underexpanded, leading to complex jet structures and possible Mach disk formation, affecting thrust. To mitigate these effects, solutions include double bell nozzles, variable geometry nozzles, and aerospike nozzles, which optimize flow expansion and efficiency across different altitudes and conditions. Studies related to the hypersonic flight are significant for several compelling reasons:

1. **Reduced Travel Time**: Hypersonic flight dramatically reduces travel time for long-distance journeys. For instance, a flight from New York to London could take less than an hour compared to the current 7-8 hours. Hypersonic flight can revolutionize global connectivity, enabling quicker delivery of goods and services. This speed can enhance global trade, emergency response, and disaster relief efforts.

2. **Enhanced Space Access**: Hypersonic technology is essential for the development of spaceplanes that can take off and land like conventional aircraft. This capability can lower the cost of access to space, streamline launch processes, and expand commercial spaceflight opportunities.

3. **Technological Innovation**: The pursuit of hypersonic flight drives advancements in various fields, including materials science, propulsion, aerodynamics, and thermal management. These innovations have the potential to benefit a wide range of industries beyond aerospace.

4. **Economic Impact**: The development and commercialization of hypersonic technology can stimulate economic growth by creating high-tech jobs, fostering new industries, and attracting investment in aerospace research and development.

5. **Military Superiority**: Hypersonic vehicles offer strategic advantages in defense. Their high speeds and maneuverability make them difficult to detect and intercept, providing a significant edge in rapid response and precision strikes.

In summary, hypersonic flight offers transformative benefits in terms of speed, military capability, space exploration, technological progress, global connectivity, and economic impact. These advantages make it a key focus of modern aerospace research and development.

Chapter 1

Mission and Goals

1.1 MORE&LESS project

The International Project MOREandLESS - MDO and REgulations for Low-boom and Environmentally Sustainable Supersonic Aviation is funded by the European Commission under the Horizon 2020 framework. This project aims to establish new standards for environmentally sustainable supersonic aviation in Europe and the broader international community. These standards will address noise, pollutants, and greenhouse gas emissions. Through a multidisciplinary approach encompassing aerodynamics, propulsion systems, emissions, and climate impact sciences, the project seeks to develop comprehensive guidelines for the European Union and the global community [12]. The project is based on LAPCAT I/II and STRATOFLY projects [13, 14, 1], vehicles designed to cruise at Mach 8 and 30 km of altitude. A re-design is under current study [15], which aimed at designing vehicles to cruise at a Mach number of 5, and an altitude of 25 km. Being in the early stage, the STRATOFLY project vehicle and LAPCAT II trajectory are described instead.

1.2 Vehicle

The concept of a hypersonic aircraft is practical primarily for long-haul routes, especially those reaching antipodal destinations, as these routes maximize the benefits of hypersonic travel. To meet the mission requirements of long-haul routes, the waverider configuration has been chosen for the STRATOFLY MR3 vehicle, ensuring a lift-to-drag (L/D) ratio higher than 6.

Liquid hydrogen is used as the propellant due to its higher specific energy compared to common carbon-based jet fuel. The use of liquid hydrogen enables complete decarbonization. Lightweight bubble structures are considered to achieve higher initial-to-final mass ratios. The STRATOFLY MR3 is designed to fly along

antipodal routes at a stratospheric altitude of about 30 km, carrying 300 passengers as payload. At elevated Mach numbers, conventional engines are no longer viable

Figure 1.1: MR3 vehicle external confguration [1].

Technical data	**Value**	**Unit of measurement**
Length	94	m
Wing span	41	m
Height	17	m
Maximum take-off gross weight	400	tons
Overall volume	10,000	m^3
Fuel weight	200	tons
Maximum thrust at take-off	3070	kN
Thrust during cruise	500	kN

Table 1.1: MR3 vehicle main technical data [1].

in terms of fuel efficiency. The combustion temperature of these engines is limited by the survival of the turbine blades. Consequently, new engine architectures must be explored. The Air-Turbo-Rocket Expander (ATR-EXP) is a turbine-based engine [16]. The core concept is to exploit the stored fuel, cryogenic hydrogen, as a coolant and working fluid while gathering air from the atmosphere as an oxidizer. This approach allows for higher combustion temperatures, similar to a rocket engine, and the absence of an oxidizer tank, as in a jet engine. The STRATOFLY propulsion plant consists of six ATR-EXP and one Dual Mode Ramjet (DMR).

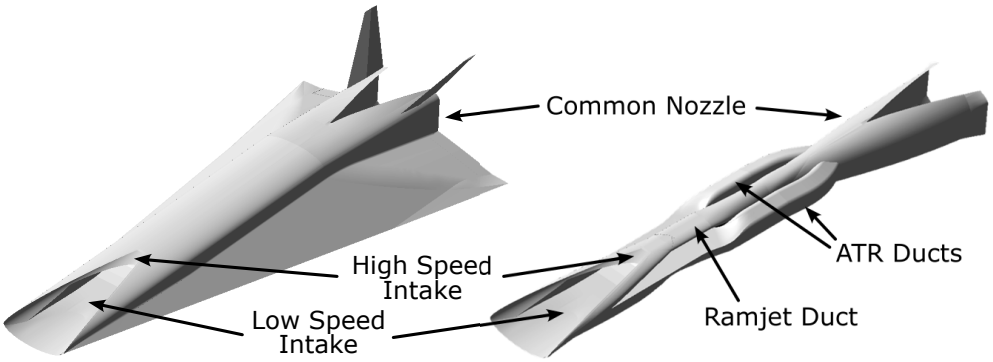

Figure 1.2: MR3 propulsive plant layout.

The six ATR-EXP engines positioned around the DMR engine, are responsible for propelling the aircraft during takeoff, subsonic cruise, and supersonic acceleration (Mach 0 to 4.5). The DMR engine, in its ramjet mode, kicks in after the aircraft reaches a cruise speed of Mach 1.5 and gradually increases its thrust contribution as the flight Mach number rises. At Mach 4.5, the ATR-EXP engines are completely shut down, and the DMR engine alone provides thrust. Both engine bays share common intake and nozzle sections. Incoming air is split into two streams, feeding the ATR-EXP engine bays and the DMR engine before the DMR isolator. The exhaust flows from both engines merge in a common nozzle downstream of the DMR combustor outlet.

The MORE&LESS project shares the same root waverider vehicle design of the STRATOFLY. Due to the early stage of design,The MORE&LESS and STRATOFLY and LAPCAT II share the same propulsion plant.

1.3 Trajectory

Figure 1.3 displays the whole trajectory and required thrust for the vehicle.

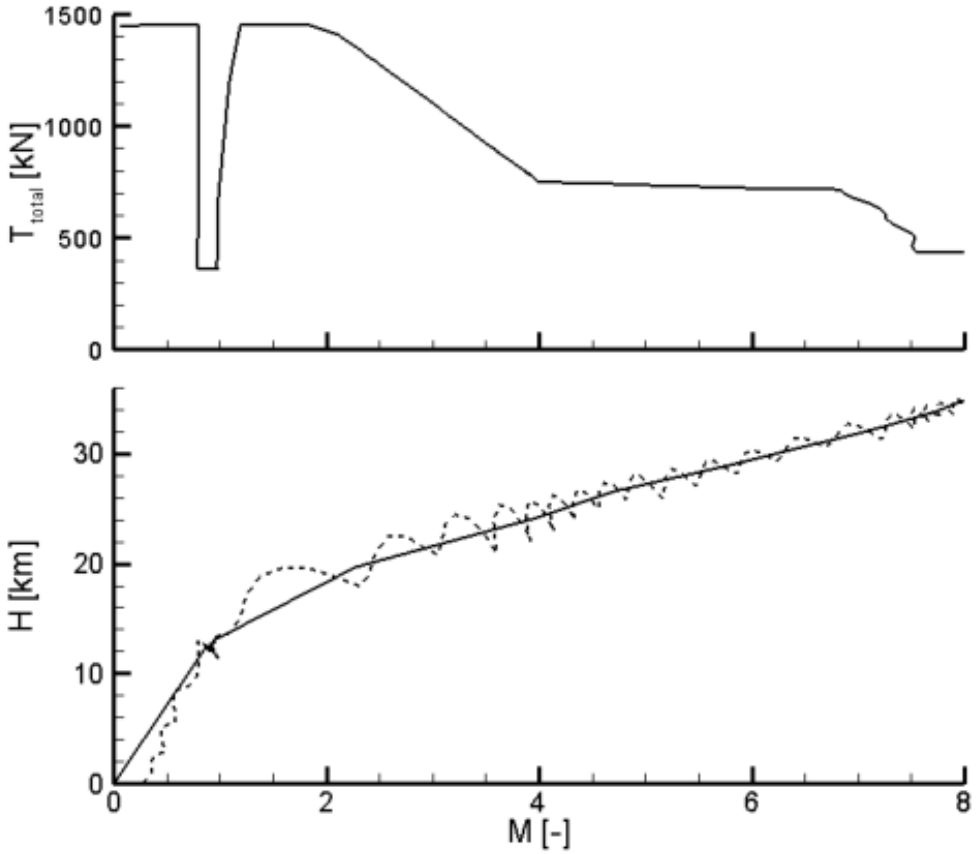

Figure 1.3: LAPCAT II trajectory [3]. The dashed line is the raw data provided by ESTEC, the solid one are used in the simulations.

The overall uninstalled thrust $F_{u_{total}}$, which is independent of the number of propulsion units, and altitude H are shown with respect to the flight Mach number M. The mission of the ATR is to accelerate from takeoff to Mach 4.5 at an altitude of 24 km, where a dual-mode ram/scramjet (DMR) further accelerates to a hypersonic cruise. The raw altitude data provided by ESTEC (dashed line) was smoothed for the simulation (solid line) [3]. For the purpose of this thesis, the trajectory has been simulated up to Mach 3, and the requested thrust has been divided by the number of engines.

1.4 Conventional cycle limitation

The figure clearly shows the performance of different conventional cycles with respect to Mach flight. The Specific Impulse is a figure of merit that measures how efficiently the chosen cycles use fuel while generating thrust [17]. A higher value represents a more efficient design. Turbofans are not capable of flying faster than

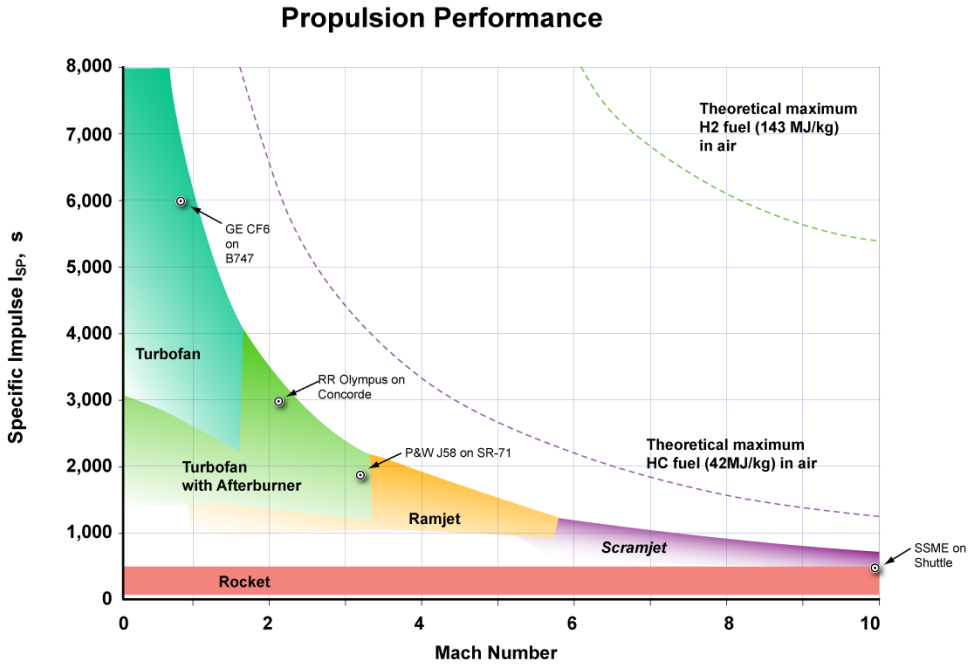

Figure 1.4: Specific Impulse over Mach number for different engines [4].

Mach 3 due to temperature constraints. Figure 1.4 illustrates that above Mach 3 the ramjet,where combustion occurs subsonically, becomes the only feasible cycle. However, beyond Mach 5, its specific impulse decreases rapidly, and the scramjet, where combustion occurs in the supersonic regime, offers a higher specific impulse at higher speeds. While the rocket's specific impulse is considerably lower than other propulsion systems, it uniquely provides operational capabilities from sea-level static conditions to beyond the atmosphere, which none of the other propulsion systems can achieve. The rocket's low specific impulse makes it unsuitable for long-range cruise, but as the Mach number increases into the hypersonic regime, the scramjet's specific impulse approaches that of the rocket engine. Optimizing for long-range, broad-speed regime operation requires the use of a combination of propulsion systems, known as combined cycle propulsion (CCP) systems. These systems adapt to various flight regimes and achieve synergistic performance enhancements over

individual cycles. Airbreathing combined-cycle engines are primarily intended for missions involving high-speed cruise in the atmosphere, with the capability to switch entirely to rocket mode for reaching orbit.

1.5 Hypersonic airbreathing propulsion

The preferred solution to the challenge of hypersonic airbreathing propulsion—achieving acceptable thrust and fuel efficiency throughout the entire flight spectrum—is to integrate multiple propulsion concepts within a single internal flow path. These airbreathing engines are referred to as combined cycles [18]. Different examples can be found in literature [19].

A classification, proposed by C. Segal [20], consists of:

- Rocket Based Combined Cycle - RBCC
- Turbine Based Combined Cycle - TBCC

The first category includes engines that can operate in rocket, ramjet, scramjet, and rocket-ejector modes. The second category can be further divided into:

- The Liquid Air Cycle Engine (LACE). The Scimitar engine is a an evolution of this concept [21]
- The Air Turbo Ramjet or Air Turbo Rocket

Based on Thomas et al. work [22], this second category is also divided into:

- Bipropellant gas generator
- Monopropellant gas generator
- Regenerative or expander cycle

Examples of the expander cycle include the ATREX by JAXA and the Air Turbo Rocket Expander engine (ATR-EXP) according to Villacé et al. work [23].

1.5.1 ATREX

The ATREX engine is the most close engine that can be compared with the ATR-EXP. The following section provides a brief description of the ATREX concept. The fuel, cryogenic hydrogen, is heated up by cooling jackets around and in the chamber and by an intake precooler before it is expanded in the turbines. The turbines power the fan and turbo pump. The hydrogen is then injected into the chamber, taking part in combustion reactions generating thrust. Cooling the

incoming air for the fan results in an inter-cooling effect on the Brayton cycle, thereby increasing both specific power and thermal efficiency. By cooling the high-temperature air—approximately 1700 K at Mach 6—the use of a turbojet system becomes feasible at high flight speeds. Additionally, adopting a tip turbine system allows for a smaller and lighter core engine. A plug nozzle is chosen because of its ability to adapt to varying conditions. The flowchart in 1.5 shows one of the first iterations of the engine. Over time, an evolution has brought differences [5], but the working principle has not changed. A smaller engine has also been tested [24].

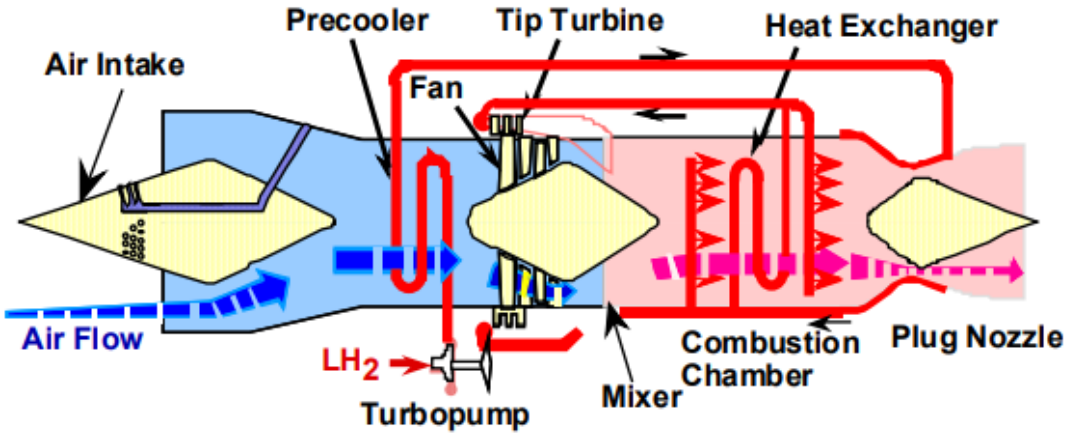

Figure 1.5: ATREX scheme [5].

1.6 Air Turbo Rocket Expander

The Air Turbo Rocket Expander engine (ATR-EXP) is a specialized type of engine that integrates features from both turbojet and rocket motors, resulting in a distinct set of performance benefits. This engine boasts a high thrust-to-weight ratio and specific thrust across a wide range of speeds and altitudes, making it an option for acceleration up to high supersonic speeds.

The engine is illustrated in 1.6. The main components of the engine are:

- Fan (F)
- Pump (P)
- Pump turbine (T1)
- Fan turbine (T2)
- Heat exchanger (HEX)
- Combustion chamber (CC)
- Nozzle (NZ)

The free-stream air enters through the inlet duct, reaching the fan. At the fan outlet, both static and stagnation pressures of the air have increased due to intake dynamic compression and the fan's work. The fan is powered by a turbine exchanging work with the fuel, i.e., hydrogen. The liquid hydrogen, stored at cryogenic conditions, passes through the turbo pump, then the heat exchanger (HEX), and then reaches the turbine. The combustion chamber and the nozzle are surrounded by a heat exchanger that cools down both of them. The regenerative heat increases the stagnation enthalpy of the hydrogen, now supercritical. The hydrogen expands through two turbines, propelling both the pump and fan. Finally, the hydrogen is introduced into the combustion chamber, where it mixes and combusts with the air from the atmosphere.

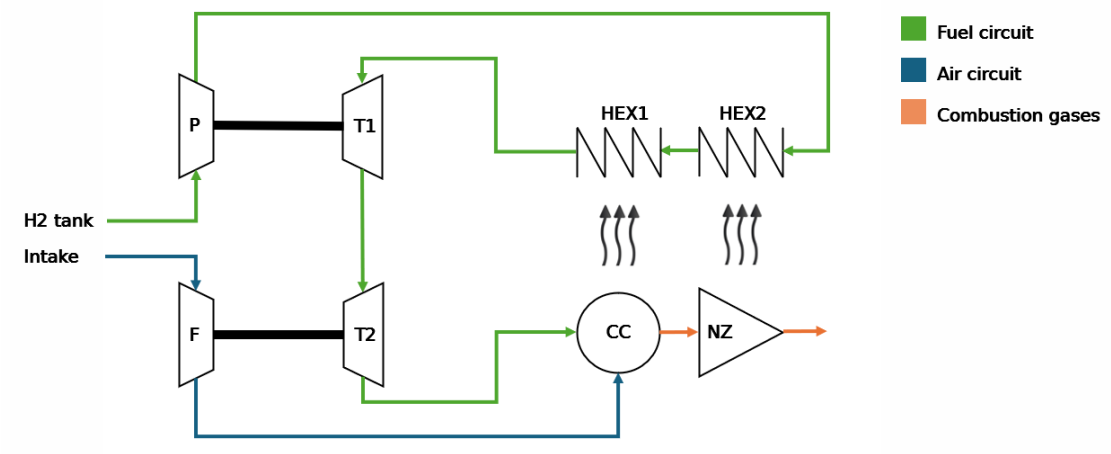

Figure 1.6: ATR-EXP engine scheme.

For control reasons, it is necessary to have two spools. To independently change the mixture ratio (MR) and the combustion chamber pressure (P_c), a power partition between the fan and pump is needed. The turbomachinery are directly connected without gearbox.

In this architecture, the cooling channels are no longer merely an accessory system to ensure engine survivability but they are the core of the engine cycle. The regenerative heat powers the engine. Indeed, the cryogenic fuel is used as a coolant, working fluid, and propellant. It is possible to think of the engine as two subsystems that work in symbiosis: the cycle powering the turbomachinery and the cycle generating thrust.

The heat exchanger represents the link between the two systems. This is clearly visible in Figure 1.6. The green lines indicate the power system, while the blue and orange lines indicate the thrust system. The power system is a Rankine cycle, whereas the thrust system is a Brayton cycle.

In Appendix A can be found a different configuration called Parallel Turbines. As the name indicates the pump and fan turbine are placed in parallel leading to differences in terms of control system and performance. Due to less engine controllability, it has been preferred to focus on the series turbine configuration. The results shown are preliminary.

1.7 Objectives

On-design studies of the propulsion plant, including the DMR, have been performed in the past [25, 26, 27] at the von Karman Institute for Fluid Dynamics. In those works, the off-design behavior of the turbomachinery was not considered. To

evaluate them, a transient model of the ATR-EXP engine and a control strategy are needed. Based on these works, the proposed goals are:

- Study how multiple actuators can be implemented inside the ATR-EXP engine architecture and their effects.
- Study a control strategy able to independently control the throttle variables through the implementation of a set of bypass valves.
- Take into account the turbomachinery off-design effects during the ascent trajectory up to Mach 3 and throttling, including operability limits and component matching.

Chapter 2

Metodology

2.1 ECOSIMPRO and ESPSS

Simulations are conducted utilizing EcosimPro [28] in conjunction with the ESPSS library. EcosimPro is a versatile, object-oriented software package designed for modeling continuous systems across various disciplines. It operates by assembling multiple individual components, each equipped with a mathematical description of its behavior, to construct a comprehensive system model. By interconnecting these components and specifying the necessary boundary conditions, a closed system of differential equations is formed, which is subsequently solved using the Differential-Algebraic System Solver (DASSL) [29]. This solver employs an implicit Newton-Raphson method, wherein the time derivative is substituted with a backward differentiation of order k. During runtime, the timestep δ_t dynamically adjusts based on the solution's evolution, facilitating the efficient integration of problems featuring both rapid and gradual temporal variations.

The ESPSS library, specializing in the simulation of spacecraft propulsion systems, provides essential components for these simulations. These components include databases pertaining to fluids, combustion chambers, turbomachinery, nozzles, and more. The combustion process is resolved using the minimum free Gibbs energy approach via the CEA solver. In this framework, air and combustion gases are modeled as mixtures of ideal gases, while hydrogen is treated as a real fluid, with its properties derived through interpolation from REFPROP tables.

2.2 Components

In ESP all physical component behaviour is mathematically encapsulated in classes. This section provides an overview of all components which are used in the engine model.

2.2.1 Ports

A connection port establishes links between components, facilitating the exchange of values required for communication with their environment. A so called "fluid" port exchanges different values among which:

- Total mass flow
- Static Temperature
- Static Pressure
- Total enthalpy

The Torque port exchanges:

- Torque
- shaft speed

The Thermal ports exchanges:

- Temperature
- Heat flux

When two or more ports are connected, equations are generated. There are two behaviors of interest:

- equal, the value at each connected port has to be the same. The speed shaft is an example.
- sum, one port flow variable is the sum of the other ports. The heat flux in a node for example.

2.2.2 Abstract components

Every component in EcoSimPro is an object in the programming sense. They can inherit the attributes and methods of the base class. Abstract components embody a physical behavior that doesn't constitute a complete component but serve as a foundation for other components by being base classes.

There are two main base classes in ESPSS fluid networks: capacity and junction. The first is a capacitive component that processes the flow variables to return the state variables as output. The second is a resistive component that receives the state variables and calculates the flow variables. Each capacitive component must be connected to a resistive component and vice versa. This computational scheme is designed to avoid algebraic loops and high-index differential-algebraic equations. The following description of components is limited to the aspects relevant to this project [30].

Capacity

This component contains the mass flow conservation equation and the energy one.

$$\frac{d\rho}{dt}V + \rho\frac{dV}{dt} = \sum_{i=1}^{N}\dot{m}_i$$

$$\frac{d\rho}{dt}Vu + \rho\frac{dV}{dt}u + \rho V du = \sum_{i=1}^{N}\dot{mh}_i + Q_{in} - PdV$$

ρ density, V Volume, $\dot{m}$ mass flow, u total specific energy, mh enthalpy flow, Q_{in} heat, P static pressure. When $\frac{dV}{dt} = 0$ and $Q_i = 0$ it is a volume.

Junction

This component embodies the fundamental abstract junction, where no mass accumulation is taken into account. Consequently, the outlet mass flow and the energy flow are preserved from changes.

$$m_{inlet} = m_{outlet}$$

$$mh_{inlet} = mh_{outlet}$$

Differently, other fluid properties (specific enthalpy and density) can change according to the following equation:

$$x = \frac{1}{2}[(1+c) * x_{upstream} + (1-c) * x_{downstream}]$$

c represent the flow direction, the reverse flow is allowed.

2.2.3 Intake

In supersonic flight, the presence of shocks induces a total pressure loss. The total pressure recovery coefficient TPR quantifies the intake's ability to slow down the air while minimizing irreversibilities:

$$TPR = \frac{p^0_{out}}{p^0_{in}}$$

To avoid instability, the external shocks cannot lay on the intake lip. Consequently, part of the air mass flow does not pass through the intake. The mass flow capture ratio is the ratio between the ideal mass flow and the real one:

$$\mu = \frac{\dot{m}_{real}}{\dot{m}_{ideal}}$$

TPR and μ can be expressed as functions of Mach number and normal shock position, describing the intake performance.

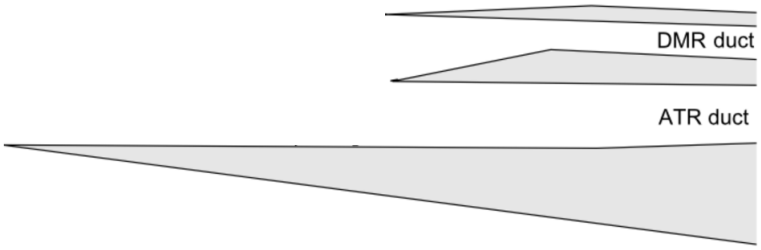

Figure 2.1: Intake sketch.

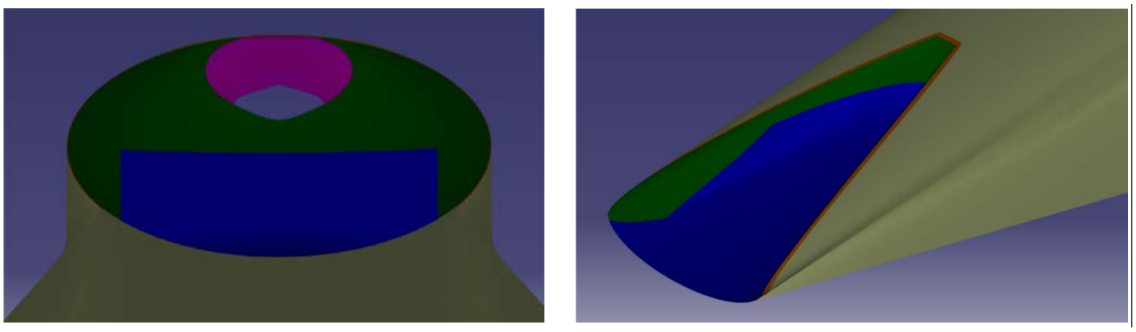

Figure 2.2: Intake front view and lateral view [6].

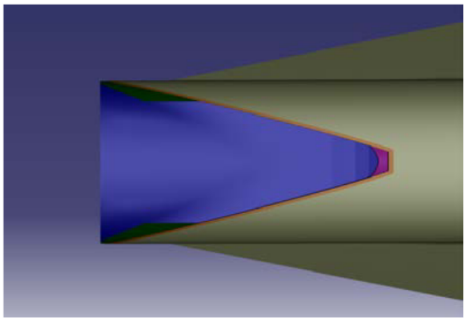

Figure 2.3: Intake top view [6].

There are two intakes for the MR2.4 vehicle concept. The first one, called the high-speed intake (HSI), is for the DMR, while the second, called the low-speed intake (LSI), feeds the ATRs. The LSI has been developed by reverse-engineering the XB-70 intake [31] [6]. The LAPCAT LSI intake is an internal-external compression

multiple shock inlet duct. It consists of three movable external ramps and three movable panels. This technology allows:

- Control of the normal shock position
- Minimization of spillage
- Maximization of total pressure recovery

It has been chosen to model the intake using only the total pressure recovery coefficient (TPR), ignoring the mass flow capture ratio (μ). This assumes that the captured mass flow rate always exceeds the mass flow rate consumed by the ATR engines. Any excess airflow is bypassed from the end of the inlet to the nozzle.

In subsonic flight, the skin friction pressure losses can be neglected, i.e., TPR is assumed to be equal to one. In supersonic flight, for the simulation, a compromise between two cases is assumed as indicated in 2.4 [32]. The worst-case scenario TPR corresponds to a theoretical calculation with no shock reflections; the optimistic case is an empirical correlation based on the XB-70 intake with shock reflections in the duct.

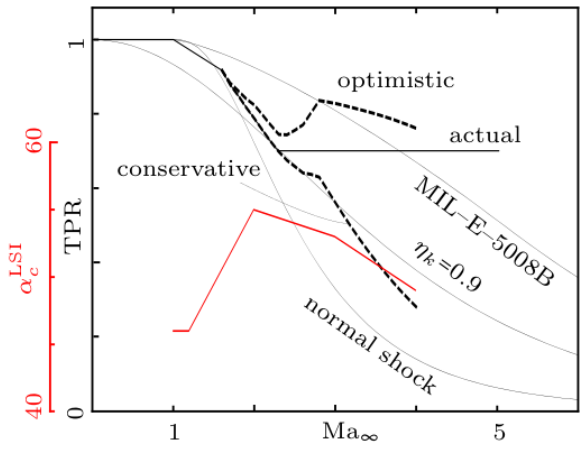

Figure 2.4: Intake total pressure recovory coefficient [7].

2.2.4 Fan and turbines

A turbomachine is a mechanical device that transfers energy between a rotor and a fluid. Our interest lies in fans and turbines. A fan is a specific class of axial compressors. An axial compressor is a rotating, airfoil-based compressor in which the gas or working fluid has an extremely limited or nonexistent radial speed component. The blades exert torque on the fluid, increasing its stagnation enthalpy

as expressed by the Euler compressor equation:

$$\dot{W}_c = \tau_A \Omega = \dot{m}(U_2 c_{\theta 2} - U_1 c_{\theta 1})$$

where:

- $\dot{W}_c$ is the rate of work done by the compressor
- τ_A is the torque applied by the blades to the fluid
- Ω is the angular rotational shaft speed
- $\dot{m}$ is the mass flow rate passing through the control volume
- U is the blade tangential speed
- c_θ is the fluid velocity component perpendicular to both the radius and the axis

An increase in temperature and pressure is a consequence of the work done by the fan. A fan is characterized by its ability to ingest large airflow with a limited compression ratio.

A turbine is a rotary mechanical device that extracts energy from a fluid flow and converts it into useful work. The following equation (Euler turbine equation) can be written for the axial type:

$$\dot{W}_t = \tau_A \Omega = \dot{m}(U_2 c_{\theta 2} - U_1 c_{\theta 1})$$

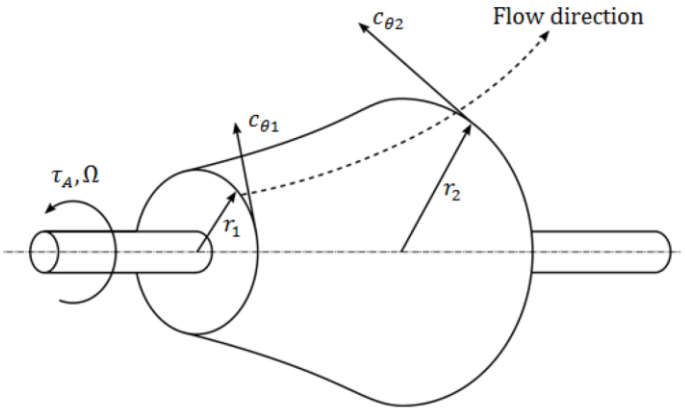

Figure 2.5: Control volume for a turbomachine [8].

The following equations are valid for both the turbine and the fan, using the subscript t for the turbine and f for the fan.

The off-design behavior of a turbomachine is described by its characteristic map. A turbomachine map is a mathematical construct that represents the functional relationships between pressure ratio, adiabatic efficiency, mass flow rate, and rotational shaft speed. Through dimensional analysis, the number of independent variables is reduced to two dimensionless numbers: corrected mass flow rate and corrected rpm.

$$N_c = \frac{N}{N_{ref}\sqrt{\theta}}$$

$$W_c = \frac{\dot{m}\sqrt{\theta}}{\delta}$$

These two variables are sufficient to express all operating conditions of the turbomachine, given the inlet stagnation temperature and pressure. The stagnation quantities are expressed with respect to the reference conditions.

$$\theta = \frac{T^0_{in}}{T^0_{ref}}$$

$$\delta = \frac{p^0_{in}}{p^0_{ref}}$$

The pressure ratio π and efficiency η are functions of corrected mass flow rate and are parameterized by corrected rpm.

$$\pi_f = \frac{P^0_{out}}{P^0_{in}} \qquad \pi_t = \frac{P^0_{in}}{P^0_{out}}$$

In ESPSS, a turbomachine is modeled as a resistive component. Two volumes are needed, one for the inlet and one for the outlet. To uniquely define a point on the map, further equations are needed to resolve the system. If the inlet and outlet conditions and a shaft torque are imposed as boundary conditions, the average of the capacity heat ratio as well as specific heat is calculated, and the outlet stagnation enthalpy is obtained. Within a timestep, the outlet stagnation enthalpy calculated has to match the stagnation enthalpy of the outlet volume. Iteratively, π and η are determined to satisfy the condition. The corrected mass flow rate and corrected rpm values were also found.

$$\gamma_{avg} = \frac{1}{2}(\gamma_{in}(P_{in}, h_{in}) + \gamma_{out}(P_{out}, h_{out}))$$

$$Cp_{avg} = \frac{1}{2}(Cp_{in}(P_{in}, h_{in}) + Cp_{out}(P_{out}, h_{out}))$$

$$h^0_{out} = h^0_{in} + Cp_{avg}T^0_{in}\left(\pi_f^{\,1-\frac{1}{\gamma_{avg}}} - 1\right)\frac{1}{\eta_f}$$

$$h^0_{out} = h^0_{in} - Cp_{avg} T^0_{in} \left(1 - \frac{1}{\pi_t^{\frac{1-\frac{1}{\gamma_{avg}}}{}}} \right) \eta_t$$

Integrating the mass balance, the mass flow rate variation is calculated. τ is a characteristic time that takes into account the fluid inertia $[m^{-1}]$ (If) and how fast the pressure waves travel.

$$\tau = \frac{(If_{in} + If_{out})R^2}{V_{sound}}$$

$$\tau \frac{d\dot{m}}{dt} = \dot{m} - \dot{m}_{in}$$

where:

- $\dot{m}$ is the mass flow calculated based on the map
- $\dot{m}_{in}$ is the inlet mass flow
- R is the characteristic blade tip radius
- V is the speed of sound

The stagnation enthalpy jump represents the power generated or requested by the turbomachinery. This power can also be viewed as mechanical power.

$$\omega \cdot Torque = \dot{m} \cdot (h^0_{out} - h^0_{in})$$

By integrating the torque balance, it is possible to determine if the spool is accelerating, decelerating, or steady.

$$I \frac{d\omega}{dt} = Torque_{port} - Torque$$

where:

- $Torque_{port}$ is the torque that other components on the same shaft are applying.

Map scaling

In a preliminary design stage, when turbomachinery needs to be developed, existing maps are scaled to evaluate engine performance [33]. Scaling ideally keeps the same component geometry while resizing it. The component map is manipulated to ensure the intended performance regardless of the physical implications induced. Commonly, linear scale factors are implemented. By choosing a point on the map, usually the on-design working point, and knowing the target values of pressure

ratio, adiabatic efficiency, and corrected mass flow rate, the scaling coefficients are calculated.

From a numerical perspective, a turbomachine map is a table. Reading it by corrected speed and corrected mass flow can be problematic at high and low speeds. To address these issues, auxiliary coordinates known as β-lines are introduced [9]. The linear coefficients K_π, K_η, and K_W are calculated as follows:

$$K_\pi = \frac{\pi - 1}{f_1(N_c, \beta) - 1}$$

$$K_\eta = \frac{\eta}{f_2(N_c, \beta)}$$

$$K_W = \frac{W_c}{f_3(N_c, \beta)}$$

where:

- $f_1(N_c, \beta)$ is the pressure ratio of the original map at the chosen scaling point identified by N_c and β.
- $f_2(N_c, \beta)$ is the adiabatic efficiency of the original map at the chosen scaling point identified by N_c and β.
- $f_3(N_c, \beta)$ is the corrected mass flow rate of the original map at the chosen scaling point identified by N_c and β.

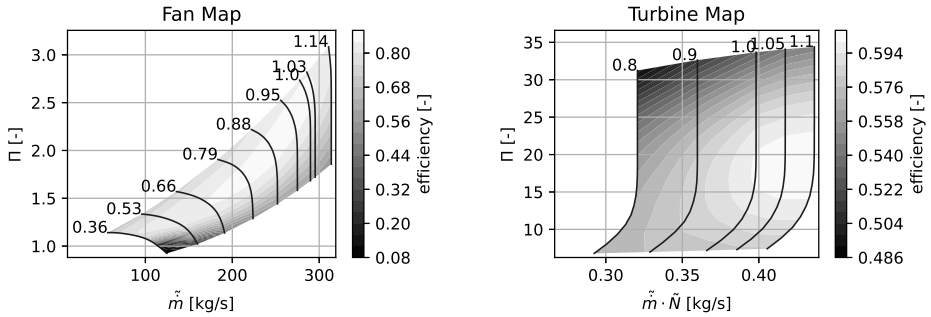

Figure 2.6: Unscaled maps used for the fans (left) and turbines (right) [9].

2.2.5 Turbo pump

Pumps can be cataloged based on specific rpm and specific diameter.

$$N_s = \frac{rpm\sqrt{Q_{ref}}}{H_{ref}^{0.75}}$$

Given the total dynamic head and the volume flow rate at reference conditions, the pump off-design performance depends on θ.

$$v = \frac{Q}{Q_{ref}}$$

$$n = \frac{N}{N_{ref}}$$

$$\theta = \pi + \arctan\frac{v}{n}$$

The efficiency and torque are tabulated as functions of N_s and θ. See the ESPSS manual [30].

$$\omega \text{ Torque} = m(h_{out}^0 - h_{in}^0)$$

This represents a power balance.

$$I\frac{d\omega}{dt} = \text{Torque}_{port} - \text{Torque}$$

$$I\frac{d\dot{m}}{dt} = P_{in}^0 - P_{pump}^0 + 9.806(H - H_{min})$$

By integrating these equations over time, the mass flow rate and rotational speed variation are calculated.

2.2.6 Combustor

The properties of an arbitrary mixture of chemicals (transport and heat capacity) are obtained from the CEA coefficients [34]. Assumed chemical equilibrium, the mass fractions and equilibrium temperature of an arbitrary mixture of reactants are derived from the Minimum Gibbs Energy Method. The injectors are modeled with a volume 2.2.2 and a junction 2.2.2 that also considers pressure losses. The momentum balance becomes:

$$(I_1 + I_2)\left(A\frac{dG}{dt} + G\frac{dA}{dt}\right) + lv\frac{dG}{dt} = P_1^0 - P_2^0 - \frac{1}{2}\left(\zeta + \zeta_{crit}\frac{G|G|}{\rho_{up}}\right) \tag{2.1}$$

where:

- P_1^0, P_2^0: stagnation pressure at inlet and outlet
- A: cross-sectional area
- I_1, I_2: half of flow inertia at inlet and outlet
- lv: small added area preventing the equation from becoming singular if $A = 0$
- G: mass flow per unit area
- ζ: pressure drop coefficient
- ρ_{up}: upstream density

The MR equation:

$$\dot{m}_{oxy} = \dot{m}_{oxy} \cdot MR + \frac{dMR}{dt} \frac{(\rho V)_{chamber}}{1 + MR} \tag{2.2}$$

The combustor is meshed in a 1D domain in the axial direction with 5 nodes. A center scheme is used to calculate the convective terms between nodes. For each node, mass and energy balance are applied:

$$V_i \frac{d\rho_i}{dt} = \dot{m}_{jun,i-1} - \dot{m}_{jun,i} \qquad i = 1, \ldots, n \tag{2.3}$$

$$\left(\frac{du_i}{dt} \rho_i + u_i \frac{d\rho_i}{dt} \right) V_i = \dot{m}h_{jun,i-1} - \dot{m}h_{jun,i} \tag{2.4}$$

where:

- $\dot{m}$: mass flow
- $\dot{m}h$: enthalpy flow
- u: volume internal energy

The chamber pressure is calculated by:

$$P_i = \rho_i R_i T_i \eta \tag{2.5}$$

where:

- η: combustion efficiency

2.2.7 Nozzle

The nozzle is a convergent-divergent type. As in the combustor chamber, it is meshed in a 1D domain in the axial direction with 2 nodes. The convergent part is considered part of the combustor. For the divergent part:

- Frozen flow condition is applied. The molar fractions of the hot gases mixture remain constant for the whole axial length of the nozzle.
- Isentropic assumption is made.

Thus, the following equations model the supersonic part.

$$\theta_i = \frac{T^0}{T_i} = 1 + \frac{1-\gamma_i}{2} M_i^2 \tag{2.6}$$

$$\delta_i = \frac{P^0}{P_i} = \theta_i^{\frac{\gamma_i - 1}{\gamma_i}} \tag{2.7}$$

Applying mass conservation between each nozzle section and the throat, given the section area it is possible to calculate the Mach number for each node.

$$M_i \frac{A_i}{A_{th}} = \left(\frac{2\theta_i}{\gamma_i + 1} \right)^{\frac{\gamma_i + 1}{2(\gamma_i - 1)}} \tag{2.8}$$

γ is a function of temperature, for each node it is valued:

$$\gamma_i(T_i) \tag{2.9}$$

Variable nozzle

Because of control needs, a nozzle with variable throat area and outlet area has been implemented using the Ecosim-Pro Language (EL). A new component has been created, allowing the simultaneous and independent change of the throat area and outlet area. During the COUNTINOUS phase, in which the differential equations are being solved, the mesh function is called to generate a new mesh. This happens at every timestep. The mesh function does not take part in the equation box but is executed sequentially.

The throat diameter, initially a DATA value that does not change during simulation, becomes a signal value received from a dedicated port. Another port is used to receive the geometrical expansion ratio value. If this value is fixed during the simulation, changing the throat diameter implies changing the outlet diameter. All the physical equations present in the standard nozzle remain the same. The throat is no longer a constraint limiting the engine but a throttle variable.

2.2.8 Heat Exchanger

Cooling of the combustion chamber and nozzle is achieved using a closed regenerative cooling system. To underline the fuel's role as a working fluid, the term "heat exchanger" is used instead of "cooling jacket". Heat exchangers are devices designed to transfer heat between two or more fluids, either to cool or heat them, without mixing the fluids. In this case, the chosen arrangement is counterflow. Fluids enter the heat exchanger at opposite ends and flow in opposite directions. This arrangement provides the highest temperature difference between fluids, improving efficiency.

The fundamental heat transfer equation used in heat exchangers is:

$$Q = UA\Delta T_m$$

where:

- Q is the rate of heat transfer,
- U is the overall heat transfer coefficient,
- A is the heat transfer area,
- ΔT_m is the mean temperature difference between the fluids.

Thus, maximizing the temperature gradient enhances the heat flow. Figure 2.7 shows a sketch of the heat exchanger in the axial direction. The inner nozzle wall is the separation surface between the two fluids, hydrogen and combusted gases. Figure 2.7 also provides a back view of the nozzle, where the cooling channels are sketched. The channels follow the nozzle's curvatures, with a rectangular cross-section and are disposed side by side along the axial direction. There is no defined design for the supply circuit, and no pressure loss of it is simulated.

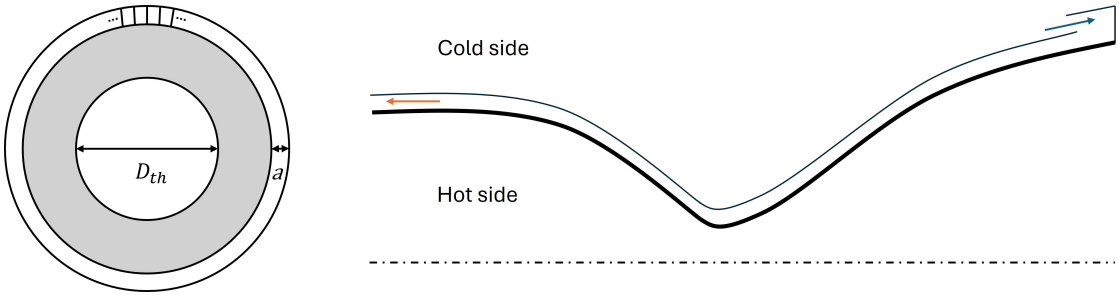

Figure 2.7: heat exchanger lateral view sketch (right) and back view (left).D_{th} is the throat diameter , a is the height of cooling channels.

All channels are aggregated into one element. This element is spatially discretized along the axial direction, with each section representing a node, for a total of 7

nodes. This more accurate model leads to a better representation of the strong hydrogen temperature and pressure variations. Each section of each channel can be represented by a thermal network as shown in Figure 2.8. As shown, the conductive heat flux between adjacent channels is considered. At the outer channel wall, an adiabatic condition is applied, so no heat flux is exchanged with the atmosphere. R_c is the conduction resistance between the faces of the same wall. R_{hv} is the convective resistance between hydrogen and walls. R_{hd} is the convective resistance between the hot gases and the nozzle wall.

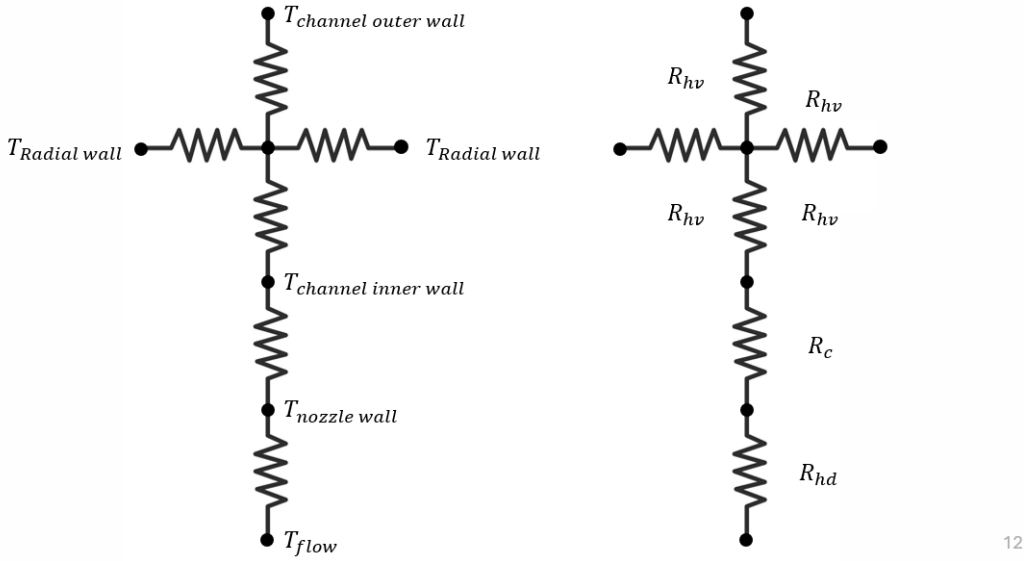

Figure 2.8: thermal network of a heat exchanger node.

Hot side

The hot side refers to the combustion gases. The mass and energy balance can be found in 2.2.6. Heat is transferred by convection and radiation.

$$q_{wall,i} = hc_i A_{wet,i}(T_{i,aw} - T_{i,act}) + qrad \qquad i = 1, ..., n$$

Convective heat transfer coefficient is model by bartz equation [35]

$$hc_i = 0.026\eta_{i,ref}^{0.2}(\lambda/\eta)_{i,ref}^{0.2} Cp_{i,ref}^{0.4} m_{th}^{0.8}/A_i^{0.9}(\pi\frac{D_{th}}{4R_{curv}})^{0.1}$$

where:

- $\eta_{i,ref}$ viscosity of burned gases at volume no. i and T_{ref} temperature
- conductivity of burned gases at volume no. i and T_{ref} temperature

- R_{curv} Curvature radius of the throat
- D_{th} Throat diameter
- m_{th} Throat mass flow
- A_i Cross section at volume no. i

The adiabatic wall temperature is the nozzle wall static temperature under adiabatic conditions. It differs from the stagnation temperature because the boundary layer, especially in supersonic flows, is not adiabatic [36]. The recovery factor relates the magnitude of the adiabatic wall temperature with the stagnation one.

$$r = \frac{T_{aw} - T}{T^0 - T}$$

where:

- T_{aw} is the adiabatic wall temperature
- T is the gas free stream static temperature
- T^0 is the gas free stream stagnation temperature

The recovery factor can be approximated with a function of Prantl number leading to the following equation for the adiabatic wall temperature:

$$T_{i,aw} = T_i(1 + Pr_{i,ref}^{0.33}\frac{\gamma_i - 1}{2}M_i^2) \qquad i = 1, ..., n$$

$$Pr_{i,ref} = (Cp_i\lambda_i/\eta_i)_{ref}$$

The difference between the adiabatic temperature and the actual nozzle wall temperature quantifies the heat flux. Radiation within the combustion chamber and nozzle is primarily caused by the presence of soot, carbon dioxide, and water vapor. However, since the concentration of carbon dioxide in atmospheric air is minimal (less than 0.4% by volume), and soot is only significant when hydrocarbon fuels are used, the radiative heat flux during the combustion of air with hydrogen is primarily influenced by water vapor. It is computed from the following expression, reported by Barrére et al. [37]:

$$q_{rad} = 4.07(\frac{p_i^{H_2O}}{98066.5})^{0.8}L_i^{0.6}((\frac{T_i}{100})^3 - (\frac{T_{w,i}}{100})^3)$$

Cold side

For each node of the coolant side, mass, momentum, and energy balances are evaluated.

$$\rho + \rho v = -\rho A k_{wall} \frac{\partial P}{\partial t} \tag{2.10}$$

$$\rho v = \rho v^2 + P + qn \tag{2.11}$$

$$\rho_u + \rho v h - \lambda \frac{\partial T}{\partial x} = -\rho u A k_{wall} (\frac{\partial P}{\partial t}) + \frac{\Delta Q}{\Delta x} + \rho g v A \tag{2.12}$$

The heat coefficient is calculated starting from the definition of the Nusselt number:

$$h_{film} = \frac{Nu\lambda}{D}$$

Depending on the flow regime, based on the Reynolds number value, the Nusselt number is estimated:

$$Nu_{laminar} = 4$$

$$Nu_{turbulent} = 0.023 Re^{0.8} Pr^{0.4}$$

The second equation is an empirical correlation known as the Dittus–Boelter equation [38]. where:

- Re Reynolds number
- Pr Prantl number

$$\Delta Q_i = h_{film,i} A_{wet,i} (T_{wall} - T_{liq}) \qquad i = 1, ..., n$$

where:

- A_{wet} lateral surface of one cooling channel section
- T_{wall} cooling channel wall temperature
- T_{liq} hydrogen temperature

A linear approximation is used for the conductive exchange inside the channel walls.

$$Q = A_{wet} \lambda (T_{outer_wall} - T_{liq}) / th$$

where:

- λ thermal conductivity

- th wall thickness

The pressure losses are considered in the momentum balance as a source term $\Delta\zeta$

$$\Delta\zeta_i = \frac{\Delta x_i}{D_i} f$$

An empirical correlation is proposed for the different flow regimes:

$$f = 8\left[(\frac{8}{Re})^{1}2 + \frac{1}{(A+B)^{3/2}}\right]^{1/12}$$

$$A = \left[2.457 \ln \frac{1}{(7/Re)^{0.9} + 0.27\epsilon/D}\right]^{16}$$

$$B = \left(\frac{37530}{Re}^{16}\right)$$

where:

- D channel hydraulic diameter
- f Darcy-Weisbach friction coefficient
- D channel hydraulic diameter
- Re Reynolds number

2.2.9 Valve

The valve is a junction as described in Section 2.2.2. It shares the same momentum balance equation with a pressure losses source term as the injector (see Section 2.2.6). The valve area is controllable value during simulation trough a signal input. The full open valve area has to be defined.

2.3 Gas models

2.3.1 Air

Air is treated as a mixture of gases modeled by the perfect gas law.

$$P = \rho \frac{RT}{MW}$$

where:

- ρ density
- R Universal Gas constant
- T Gas temperature
- MW molecular weight

The specific heat at constant pressure is a function of temperature that interpolate CEA database.

$$\frac{Cp}{R} = a_1 T^{-2} + a_2 T^{-1} + a_3 + a_4 T + a_5 T^2 + a_6 T^3 + a_7 T^4$$

Enthalpy and entropy are calculated by

$$H = H(T_0) + \int_{T_0}^{T} Cp(T) dT$$

$$S = S(T_0, P_0) + \int_{T_0}^{T} \frac{Cp(T)}{T} dT - \frac{R}{MW} \log(P/P_0)$$

Viscosity and thermal conductivity are temperature functions. Being a mixture the properties are calculated with linear mixing rules assuming the same temperature for all constituents.

$$x_k = \frac{\rho_k}{\sum_{k=1}^{nchem} \rho_k}$$

x_k is the molar fraction of each components. H, S, Cp, Cv of the mixture are calculated as following

$$y = \sum_{k=1}^{nchem} y_k x_k$$

The atmosphere pressure changes over the altitude are considered trough the international standard atmosphere [39].

2.3.2 Hydrogen

Hydrogen is treated as a real fluid, and for a given pair of temperature and pressure, all fluid properties are obtained by table interpolation. Ortho hydrogen has been used, even though the storing temperature and pressure are 21 K and 3 bar. The tables are generated based on the REFPROP database [40].

2.4 PI controller

A Proportional-Integral (PI) controller is a common control mechanism used in various engineering applications to regulate the behavior of dynamic systems. It is designed to improve the stability and performance of processes by minimizing the error between a desired setpoint and the actual output of the system.

$$u(t) = K_p e(t) + K_i \int_{\delta_t} e(t)dt$$

where:

- $u(t)$ is the control output at time t,
- K_p is the proportional gain,
- K_i is the integral gain,
- $e(t)$ is the error at time t, which is the difference between the setpoint and the measured process variable.

The proportional control term helps provide a prompt reaction to error but does not eliminate it completely, leading to a steady-state error. The integral term accounts for the accumulation of past errors. Integrating the error eliminates the steady-state error but can lead to a wind-up issue. This problem arises when the integral term of the PI controller accumulates a large error over time, leading to excessive overshoot or prolonged response times. An integral clamping scheme is implemented to avoid wind-up. When the control output $u(t)$ reaches its limit, the integral term is frozen, preventing further accumulation. This technique involves adjusting the integral calculation to exclude periods when the actuator is saturated:

$$\int_0^t e(\tau)d\tau = \int_0^{t'} e(\tau)d\tau$$

2.5 Engine Model

Figure 2.9 shows the exact engine model implemented with all the volumes (C) and junctions (J). CCN1 is the combustion chamber and nozzle. The boxes highlight the control modules implemented.

1. bypass pump turbine
2. heat capture control
3. bypass fan turbine
4. injectors control
5. throat area and aspect ratio control

2.5.1 Model Limitations

Although the simulation is transient, some aspects have been simplified in the modeling approach that could further enhance the accuracy with which the transient engine behavior is captured.

- The maps used in the modeling of the turbomachinery describe the steady off-design performance and loss of accuracy during quick transients. Additionally, heat-soakage effects and varying tip gaps due to differential cooling of the blades and casing are not included. However, this method is still often implemented in literature sources [9, 41], hence it was deemed sufficient for this study, where the main purpose is to investigate practical control strategies.
- Transients in mass flow rate will cause changes in the inlet shock structure, altering the total pressure recovery ratio (TPR) and the mass flow capture ratio during the engine transient. These transients could also lead to inlet unstart. These effects have not been taken into account, starting from the assumption that a bypass duct will divert all excess airflow from the inlet to the nozzle. Furthermore, the transients in mass flow rate are assumed to occur sufficiently slowly.
- The volumes and spool inertias have not been assessed in detail. As such, the transient times are not accurate compared to what would occur in a real fabricated engine. The conclusions drawn from the control studies should still remain valid. An accurate assessment of the spool inertias and volumes is planned for a follow-up project, where the turbomachinery components will be subjected to detailed design. This will also increase the suitability of the specific turbomachinery maps used.

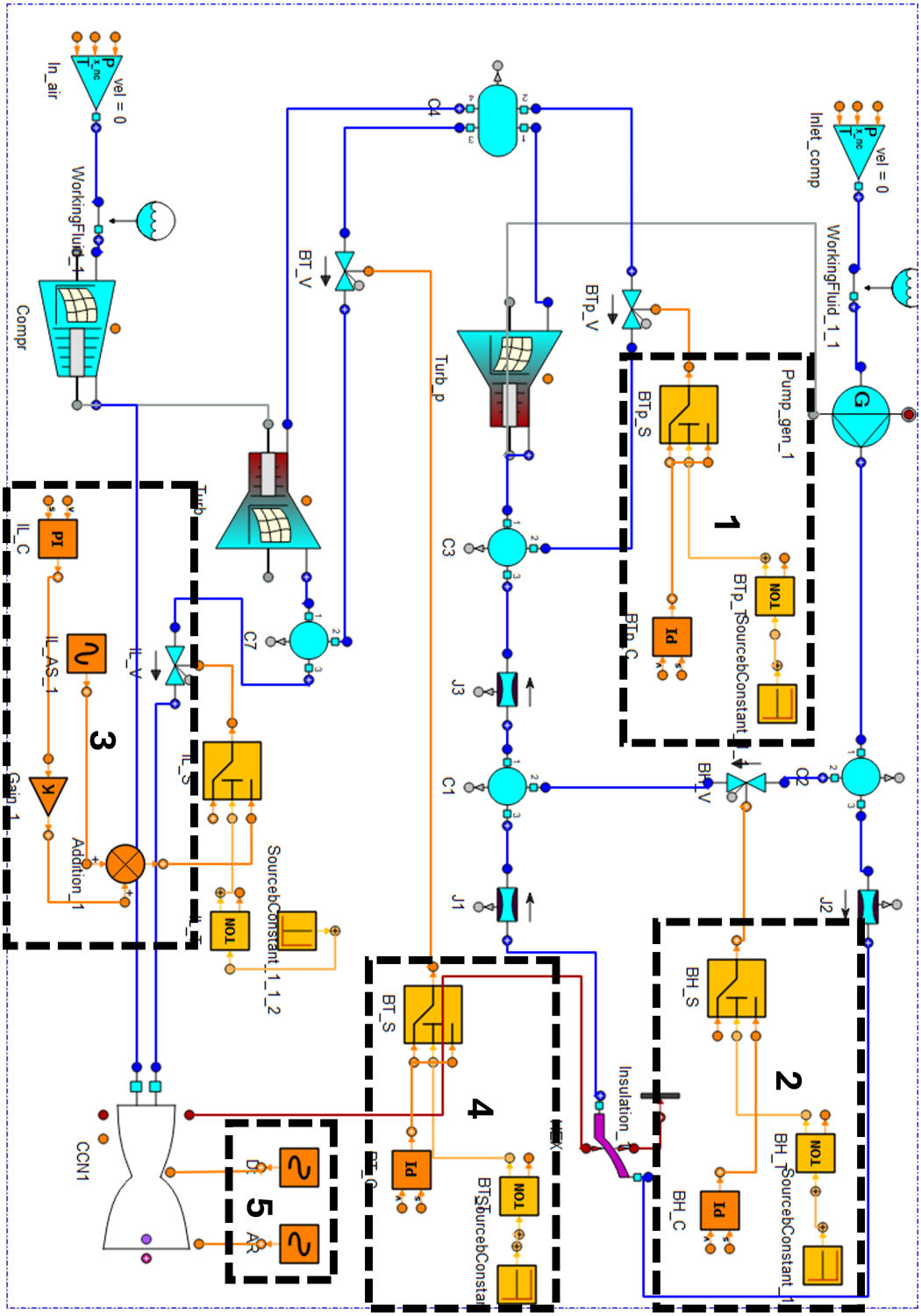

Figure 2.9: Engine schematic.

2.6 Genetic Optimization Algorithm

This section refers to the steady state optimization conducted previously at Von Karman Institute. The data produced is the foundation of this thesis; therefore, it was decided to briefly address how it was obtained. A single-objective optimization of the ATR engine's fuel consumption is conducted using Computer-Aided Design and Optimization tool (CADO) [42]. This process employs a differential evolutionary algorithm, which is non-gradient based. The algorithm mimics Darwinian natural selection, where a population of individuals evolves to better adapt to their environment. It uses numerical methods to replicate natural processes such as mutation, crossover, and selection. Being a gradient-free method, this approach necessitates a relatively large number of function evaluations compared to gradient-based methods, making it less suitable for problems with numerous optimization parameters. In this algorithm, each design, referred to as an individual, is assessed within a population T. An individual is represented as a vector of length n corresponding to the n design variables.

$$x^t = (x_1, x_2 ... x_n)$$

Three individuals a^t, b^t and c^t are randomly chosen from the population to evolve the individual and form the trial vector y. This evolution is carried out using a mutation operator, which is defined as follows:

$$y_i = a_i + F(b_i - c_i) i = 1, ..., n$$

The amplification factor F changes with generations, with smaller values reaching convergence. The recombination operator is responsible for the individuals of next generation.

$$z_i = \begin{cases} y_i & \text{if } r_i > C \\ x_i & \text{if } r_i < C \end{cases}$$

With r_i a randomly generated number. The crossover constant C determine if the new gene y_i will be present in a new individual z_i of the next generation. The new individual is evaluated and the selection operator decide if it will survive or not.

$$x_i^{t+1} = \begin{cases} x_i^t & \text{if } f(x_i^t) < f(z) \\ z_i & \text{if } f(x_i^t) \geq f(z) \end{cases}$$

The design variables are the nozzle throat area, combustor pressure and mixture ratio.

2.7 Throttle variables

This section is based on the work of Miranda et al. [16], with a detailed description of the equations modified to model a two-shaft engine. To understand which variables have a major impact relative to others, and which ones are worth controlling, it is essential to take a step back. In this section, a mathematical model of the engine cycle is proposed to demonstrate which variables can be chosen to throttle the engine. The following equations are not actually implemented in the engine schematic.

$$\Delta h_f = \frac{T^0_{amb} C_{P_f}}{\eta_f} \left(\pi_f^{\frac{\gamma_f - 1}{\gamma_f}} - 1 \right) \tag{2.13}$$

$$\Delta h_p = \frac{T^0_{tank} C_{P_p}}{\eta_p MR} \left(\pi_p^{\frac{\gamma_p - 1}{\gamma_p}} - 1 \right) \tag{2.14}$$

MR (mixture ratio), π compression ratio, η isentropic efficiency.

$$MR = \frac{\dot{m_{air}}}{\dot{m_{H2}}} \tag{2.15}$$

$$\eta = \frac{\Delta h_s}{\Delta h} \tag{2.16}$$

$$\pi = \frac{p^0_e}{p^0_i} \tag{2.17}$$

In 2.18, the MR is present because everything is referenced to $\dot{m}_{\text{air}}$, but the pump is only crossed by the fuel. The same can be said for the turbines.

$$\Delta h_t = \eta_t \frac{T^0_{i,t} C_{P_t}}{MR} \left(1 - \left(\frac{1}{\pi_t} \right)^{\frac{\gamma_t - 1}{\gamma_t}} \right) \tag{2.18}$$

$$\eta_t = \frac{\Delta h}{\Delta h_s} \tag{2.19}$$

$$\pi_t = \frac{p^0_i}{p^0_e} \tag{2.20}$$

To model the heat exchanger (HEX), it is necessary to introduce q_h [J/kg] representing the specific heat capture and δ_h for the percentual pressure drop. Equation 2.21 provides the definition, while Equation 2.22 is a convenient rearrangement.

$$\delta_h = \frac{p^0_i - p^0_e}{p^0_e} \tag{2.21}$$

$$\frac{p^0_e}{p^0_i} = \frac{1}{1 + \delta_H} \tag{2.22}$$

It is still necessary to define C_p as the specific heat and the specific heat ratio γ. In steady-state, five equations are in place. The energy balance states that the energy generated by the turbines drives the fan or pump. First spool energy balance:

$$\Delta h_p = \Delta h_{t1} \tag{2.23}$$

$$\frac{T^0_{tank} C_{P_p}}{\eta_p MR} \left(\pi_p^{\frac{\gamma_p - 1}{\gamma_p}} - 1 \right) = \eta_t \frac{T^0_{i,t} C_{P_t}}{MR} \left(1 - \left(\frac{1}{\pi_t} \right)^{\frac{\gamma_t - 1}{\gamma_t}} \right) \tag{2.24}$$

Second spool energy balance:

$$\Delta h_f = \Delta h_{t2} \tag{2.25}$$

$$\frac{T^0_{amb} C_{P_f}}{\eta_f} \left(\pi_f^{\frac{\gamma_f - 1}{\gamma_f}} - 1 \right) = \eta_t \frac{T^0_{i,t} C_{P_t}}{MR} \left(1 - \left(\frac{1}{\pi_t} \right)^{\frac{\gamma_t - 1}{\gamma_t}} \right) \tag{2.26}$$

The pressure balance conveys the fact that in the combustion chamber, both the airflow and fuel have the same pressure P_c. Pressure balance:

$$p^0_\infty TPR \pi_f = p^0_{tank} \pi_p \frac{1}{1 + \delta_H} \frac{1}{\pi_{t1}} \frac{1}{\pi_{t2}} \tag{2.27}$$

With TPR being the intake recovery efficiency. In 2.28, the heat exchanger is treated with the same logic as a combustion chamber, just without specifying the origin of the heat. In the case of a combustion chamber, it would be the chemical energy in the fuel; here, it is the fraction conveyed by the HEX. Energy capture:

$$T^0_{i,t1} = \frac{C_{P_p}}{C_{P_{t1}}} T^0_{tank} \left(1 + \frac{\pi_p^{\frac{\gamma_{t1} - 1}{\gamma_{t1}}}}{\eta_p} \right) + \frac{q_H}{C_{P_t}} (MR + 1) \tag{2.28}$$

Combustion energy balance:

$$LHV = MR \Delta h_{ch} + q_h \tag{2.29}$$

$$T^0_c = \frac{LHV}{MRC_{p_c}} + \frac{T^0_{i,t2}}{\pi_{t2}^{\frac{\gamma_{t1} - 1}{\gamma_{t1}}}} + q_h \frac{MR + 1}{MRC_{p_c}} \tag{2.30}$$

Equation 2.30 underscores how a portion of the chemical energy flows through the HEX, while the rest contributes to thrust. To close the system, Equation 2.31 is introduced, stating that the outlet stagnation temperature of the first turbine is the inlet of the second one.

$$T^0_{i,t2} = T^0_{i,t1} \pi_{t1}^{\frac{\gamma_{t1} - 1}{\gamma_{t1}}} \tag{2.31}$$

Considering:

- the efficiencies (η,TPR) , the flight conditions (p_∞,M_0) and the storage condition (T^0_{tank},p^0_{tank}) fixed

- specific heat (C_p) and capacity heat ratio (γ) and lower heat value (LHV) known at each station

It is a system with 6 equations and 10 variables:

$$(\pi_f, \pi_p, \pi_{t1}, \pi_{t2}, \delta_h, T^0_{i,t2}, T^0_{i,t1}, T^0_c, MR, q_h)$$

To close the system, 4 variables must be fixed. The chosen variables are P_c, MR, q_H, and δ_H. These variables define the cycle. Defining a cycle means generating a family of engines because the cycle is referenced to specific quantities, i.e., enthalpy and entropy are per kg/s of flow. Once a cycle is defined, it is possible to calculate the exit flow speed using Equation 2.33, thus determining the specific thrust. It can be demonstrated that T^0_c, γ, and R_{gas} are functions of MR. Dividing the uninstalled thrust required by F_{sp} will define an engine.

$$V_e = \sqrt{\frac{2\gamma R_g T^o_c}{\gamma - 1}(1 - \frac{p_{amb}}{p^o_c}^{\frac{\gamma-1}{\gamma}})} = g(p^o_c, MR) \tag{2.32}$$

$$F_{sp} = \frac{F_u}{\dot{m}_{air}} = [(1 + \frac{1}{MR})V_e\eta_n - V_\infty] \tag{2.33}$$

$$\dot{m}_{th} = \frac{p^o_t A_{th}}{\sqrt{R_g T^o_c}} f(M = 1) = h(p^o_c, MR, A_{th}) \tag{2.34}$$

To exploit the supersonic expansion inside the divergent nozzle, the throat must be choked. Thus, the thrust F_u is limited by the size of A_{throat} as shown in 2.35.

$$F_u = \dot{m}_{air}[(1 + \frac{1}{MR})V_e\eta_n - V_\infty] \tag{2.35}$$

The HEX geometry is defined, thus the HEX pressure drop, which is a function of it, cannot be considered a throttle variable. It is now clear that the focus of our research is to control MR, P_c, and A_{throat}, as these directly impact thrust. Conveniently, the first two also affect the cycle, influencing the work and thermal efficiency of the engine. Controlling these variables means controlling the engine. Furthermore, conceptually, MR is intimately related to fuel consumption, P_c is measurable during tests, and A_{throat} is a geometrical feature. It is reasonable to think that having three variables allows for an optimal combination in terms of

efficiency relative to others. The following figures of merit are used to assess this:

$$I_{sp} = \frac{F_u}{\dot{m}_{H2} g} = \frac{1}{TSFC g} \tag{2.36}$$

$$\eta_{th} = \frac{2 F_u V_\infty}{\dot{m}_{th} V_e^2 - \dot{m}_{air} V_\infty^2} \tag{2.37}$$

$$\eta_p = \frac{\dot{m}_{th} V_e^2 - \dot{m}_{air} V_\infty^2}{2 \dot{m}_{H2} LHV} \tag{2.38}$$

$$\eta_o = \frac{F_u V_\infty}{\dot{m}_{H2} LHV} = \eta_{th} \eta_p \tag{2.39}$$

2.8 Validation

This thesis aims to demonstrate the controllability of the engine with the aforementioned throttle variables. Given the interest in simulating the ascent trajectory, a specific individual from an initial flight condition was chosen. The best individual resulting from the optimization has been selected.

After choosing the individual, the first step was to replicate the steady results within the off-design model. To achieve this goal, the system was initially broken apart into subsystems as the fuel circuit and the air circuit. The last step was to assemble each subsystem and test the overall system. Forty-seven variables were evaluated to assess the match, focusing on the most important components: turbo machinery, heat exchanger, and combustion chamber.

Studying only one ATR-EXP instead of the entire propulsion plant (including the DMR) required redesigning the nozzle. Consequently, the geometries of the heat exchanger changed. These changes led to different pressure losses, 8% lower concerning the steady reference case. Pressure losses in the injectors also contributed to a different stable condition. Additionally, various difficulties were encountered in scaling the turbines, as the steady-state model only included one. In the steady reference, only one turbine has been modeled for both pump and fan. This has been possible because only power matching has been performed- For engine control purposes, it is beneficial to split the turbine into two, one powering the pump and one powering the fan. As this allows for more flexibility. As such, steady results could not directly be used for the map scaling. The thrust presents an error of less than 1%, while the chamber pressure (P_c) has an error of -2%. The mixture ratio error is -9%.

Lower pressure losses led to a higher hydrogen flow rate, while errors in scaling the fan resulted in a lower air flow rate. The throat area is fixed. In this case, validation resulted in a lower specific impulse. In general, the errors are always under 10% except for the fan turbine outlet pressure as a combined result of map scaling and differences in HEX pressure losses. This result has been considered acceptable.

	TARGET	RESULT	UNITS	ERROR
Turb.Ncorr	1.00	1.02	-	2%
Turb.beta	0.50	0.50	-	-1%
Turb.pi	DNF	14.34	-	-
Turb.eta	0.60	0.60	-	0%
Turb.Power	-5.28E+07	-4.91E+07	W	-7%
Turb.Tt_in	DNF	494	K	-
Turb.Tt_out	349	337	K	-3%
Turb.Pt_in	DNF	5.89E+06	Pa	-
Turb.Pt_out	3.21E+05	4.11E+05	Pa	28%
Turb.mflow	20.03	21.27	kg/s	6%
Turb_p.Ncorr	1.00	1.06	-	6%
Turb_p.beta	0.50	0.55	-	11%
Turb_p.pi	DNF	1.15	-	-
Turb_p.eta	0.60	0.60	-	0%
Turb_p.Power	-3.38E+06	-3.64E+06	W	8%
Turb_p.Tt_in	539.01	505.30	K	-6%
Turb_p.Tt_out	DNF	493.98	K	-
Turb_p.Pt_in	6552053.58	6754712.58	Pa	3%
Turb_p.Pt_out	DNF	5894007.61	Pa	-
Turb_p.mflow	20.03	21.27	kg/s	6%
Compr.Ncorr	1.00	0.98	-	-2%
Compr.beta	0.50	0.53	-	5%
Compr.pi	2.47	2.42	-	-2%
Compr.Power	5.28E+07	4.91E+07	W	-7%
Compr.Tt_in	308	308	K	0%
Compr.Tt_out	411	407	K	-1%
Compr.Pt_in	1.13E+05	1.13E+05	Pa	0%
Compr.Pt_out	2.81E+05	2.74E+05	Pa	-2%
Compr.mflow	508	489	kg/s	-4%
Pump_gen_1.Power	3.38E+06	3.64E+06	W	8%
Pump_gen_1.f2.P	8.95E+06	8.98E+06	Pa	0%
Pump_gen_1.f2.Tup	29.77	29.99	K	1%
Turb.sh_out.omega	400.03	390.03	rad/s	-2%
Turb_p.sh_out.omega	400.03	410.97	rad/s	3%
HEX.f2.m	2.00E+01	2.13E+01	kg/s	6%
HEX.f1.Tup	5.41E+02	5.05E+02	K	-7%
HEX.f1.P	6.51E+06	6.74E+06	Pa	3%
hex_p	1.46E+08	1.45E+08	W	-1%
HEX.Channel.dP_loss	-2.42E+06	-2.24E+06	Pa	-8%
CCN1.Inj_oxy.dP_loss	1.34E+04	1.26E+04	Pa	-5%
CCN1.Inj_red.dP_loss	5.35E+04	5.84E+04	Pa	9%
CCN1.Combustor.P[1]	2.67E+05	2.61E+05	Pa	-2%
CCN1.Combustor.T[1]	2214.67	2305.12	K	4%
CCN1.Combustor.MR	25.38	23.00		-9%
CCN1.Combustor.m_jun[1]	528.34	510.50	kg/s	-3%
CCN1.Combustor.Dt_s.signal[1]	1.89	1.89	m	0%
thrust	384074.61	390193.06	N	2%

Figure 2.10: Table comparison between engine steady-state model with engine transient model in steady-state.

Figure 2.11 and 2.12 shows a transient simulation at Mach 0.75. The simulation starts with the engine operating point different from the equilibrium one causing the transient. The engine in this simulation is without any kind of control. After the initial speed up the shafts reach the maximum speed at the thrust outputs remain constant. Proving the open-loop stability at least in this trajectory point.

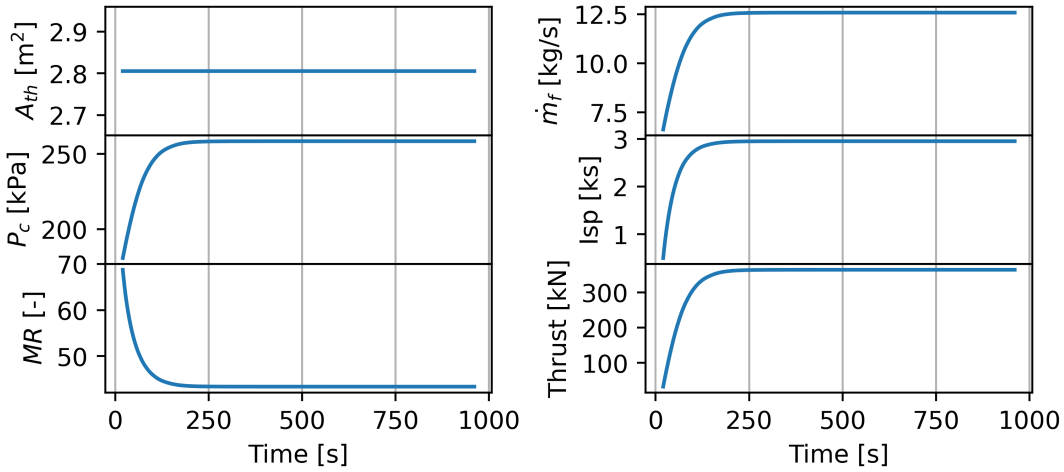

Figure 2.11: Mach 0.75, system without control, throttle variables and $\dot{m}_f$, I_{sp}, thrust over time.

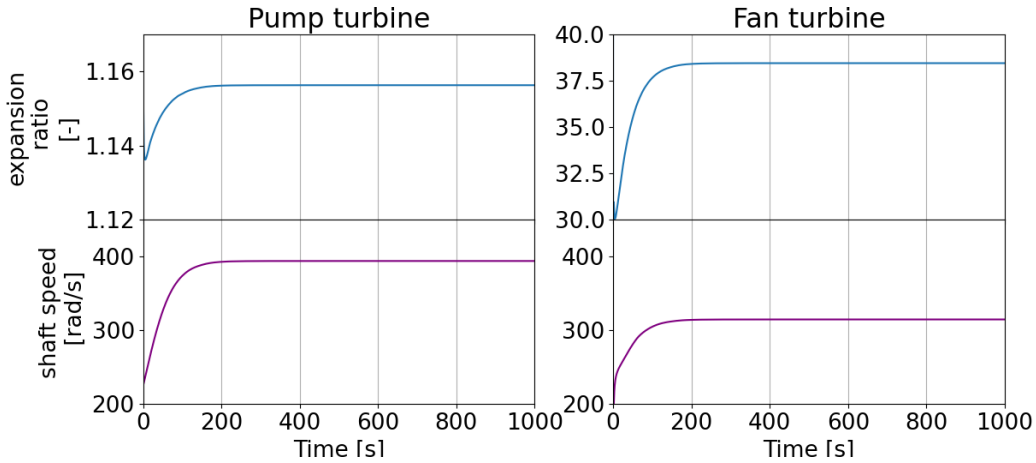

Figure 2.12: Mach 0.75, system without control, pump turbine expansion ratio and speed shaft over time and fan turbine expansion ratio and speed shaft over time.

Chapter 3

Control Strategies

Some adjustments have to be made to control the engine. The validation described in section 2.8 was performed in open-loop, demonstrating that, at least for this operating condition, the engine is inherently stable. The mixture ratio (MR) and combustion chamber pressure (P_c) are the throttle variables, along with the throat area. At first glance, based on the definition in equation 2.16, to control the MR, the mass flow rate of the air or the hydrogen has to change. The fuel circuit load pressure or the turbo pump working point influences the fuel flow, while the fan working point influences the airflow. The P_c depends on the fan compression ratio; the chamber pressure is imposed by the air pressure minus the injector losses. Two options are available to control the P_c: changing the fan working point or changing the air injector size. Thus, even if MR and P_c are throttle variables, with the feedback loop passing these variables as set signals for the controllers, the actuators will change other parameters to achieve the desired effects.

We are now interested in understanding which kinds of actuators can be implemented and quantifying their effects first on the fuel circuit and then on the throttle variables, as discussed in section 3.5. The throat area can be modified directly. On a shaft, the turbine provides energy for the fan in according to the energy balance equation 2.24. Consequently, moving the turbine working point means a variation in turbine power and a shift in the fan working point. This is also true for the turbo pump. Changing the turbine's working points induces a shift in turbopump and fan working points.

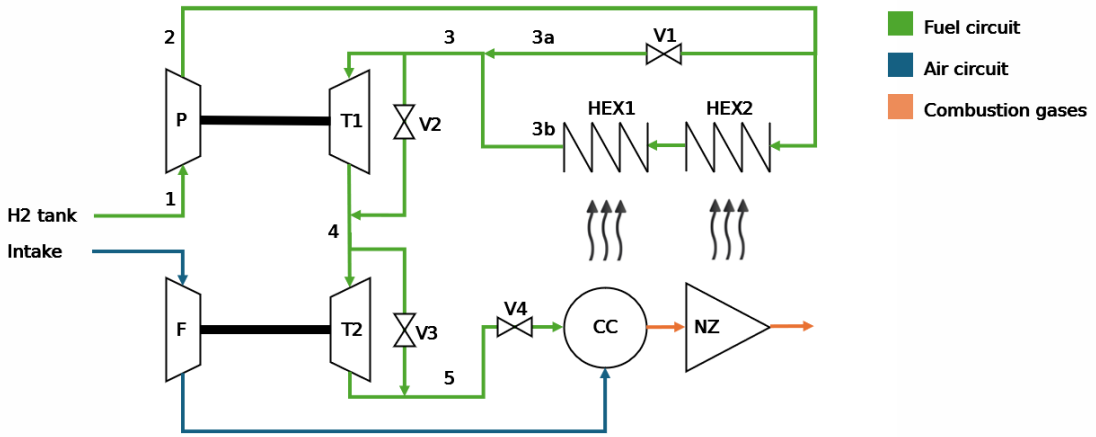

Figure 3.1: engine scheme with actuators.

Multiple are the options to change the turbines power output, within this engine cycle described in section 1.6:

- cut the energy source by lowering the turbine inlet total temperature.
- diverting part of the fuel mass flow rate away from the turbine with a bypass valve.
- modifying the fuel circuit pressure losses, hence the fuel flow by moving the turbo pump working point.

During flight, valves can be used as actuators to accomplish these options. For each throttle variable, an actuator must be in place. The position of the valve on the fuel circuit affects the overall system. There are four strategic positions where the valves can be placed, as shown in Figure 3.1.

- bypass HEX (V1) actuating the first option
- in line valve (V4) implementing the third option
- bypass Pump Turbine (V2) realizing the second option
- bypass Fan Turbine (V3) performing the second option

Each valve in its strategic position is a control strategy. Each control strategy can be assigned to one throttle variable. Having the throat area directly imposed, and being interested in controlling P_c and MR, two control strategies must work together, forming a control system. Different control strategy combinations, i.e. control systems, can exist which will be discussed in section 4.

To evaluate the effects of opening and closing of each valve a study is conducted. It has been performed as follows: starting from Mach 0.75, the engine described in section 2.8 is brought to Mach 2. Once steady-state conditions are reached, the control system is shut off.

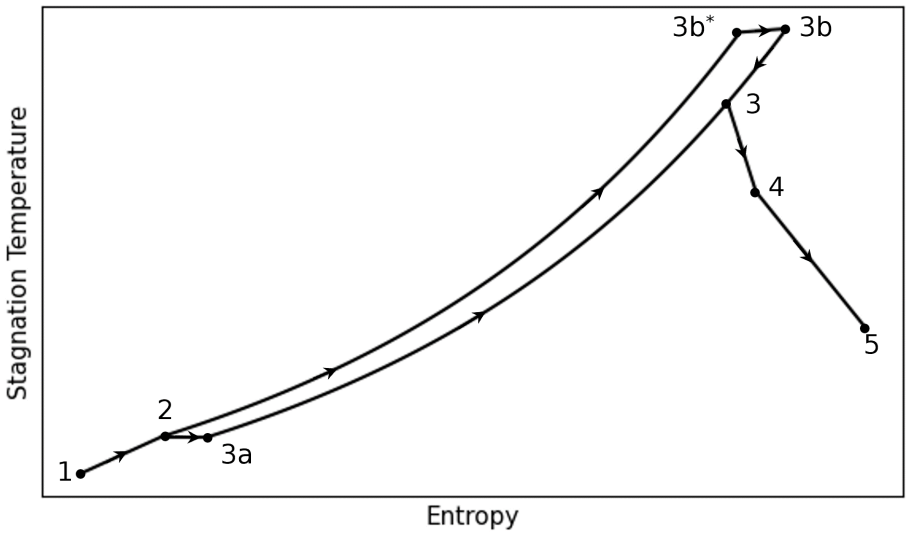

Figure 3.2: Fuel circuit stations on T-S chart.Station 1 and 2 are respectively inlet and outlet pump. Point 3a is the outlet of valve V1, the heat exchanger (HEX) bypass. Point 3b^* is the HEX outlet without considering the pressure losses inside it. Point 3b is the actual HEX outlet. Point 3 is the volume where the bypassed hydrogen flow encounter the one passed through the HEX. Point 4 and 5 are respectively the pump turbine outlet and the fan turbine outlet.

One valve is kept in the same position, while the other is perturbed by a certain percentage of its initial position. For each control strategy, the corresponding control system is used, as described in section 4. For the pump turbine, the test is conducted with both turbines bypassed (CS1). In Figure 3.1 the fuel circuit stations are shown. Station 1 and 2 are respectively inlet and outlet pump. Point 3a is the outlet of the V1 valve, the heat exchanger (HEX) bypass. Point 3b^* is the HEX outlet without considering the pressure losses inside it. Point 3b is the actual HEX outlet. Point 3 is the volume where the bypassed hydrogen flow encounters the one passed through the HEX. Point 4 and 5 are respectively the pump turbine outlet and the fan turbine outlet. The entropy and stagnation temperature are shown in Figure 3.2. The T-S chart shows the case when V1 is not completely closed. The chart is intended to show each transformation to which hydrogen is

subjected. If V1 is completely closed, point 3*b* collapses on point 3 as shown in Figure 3.5.

In the following subsections, each chart presents three cycles. To qualitatively assess the effect of the valve position for each control actuator, three valve positions are evaluated. The blue case represents the most closed position, the green one the most open, and the orange one represents a valve opening between the two. Indeed, the valve opens progressively from the blue case to the green one. In the case of a bypass valve, as the valves open a pressure drop is introduced and fuel flow is deflected. In the case of the in line valve control the valve opening reduces the fuel circuit pressure losses. The throat area is kept constant.

3.1 Heat Capture Control

A bypass valve (V1) is placed parallel to the heat exchanger. For a fixed inlet temperature and fixed wall temperature, depending on the fuel mass flow rate, the Reynolds number will change, affecting the heat transfer coefficient on the coolant side as shown in Figure 2.2.8. In this way, it is possible to control the heat capture and consequently the turbines' operating points. Additionally, providing an easier passage with less flow resistance diverts part of the fuel flow.

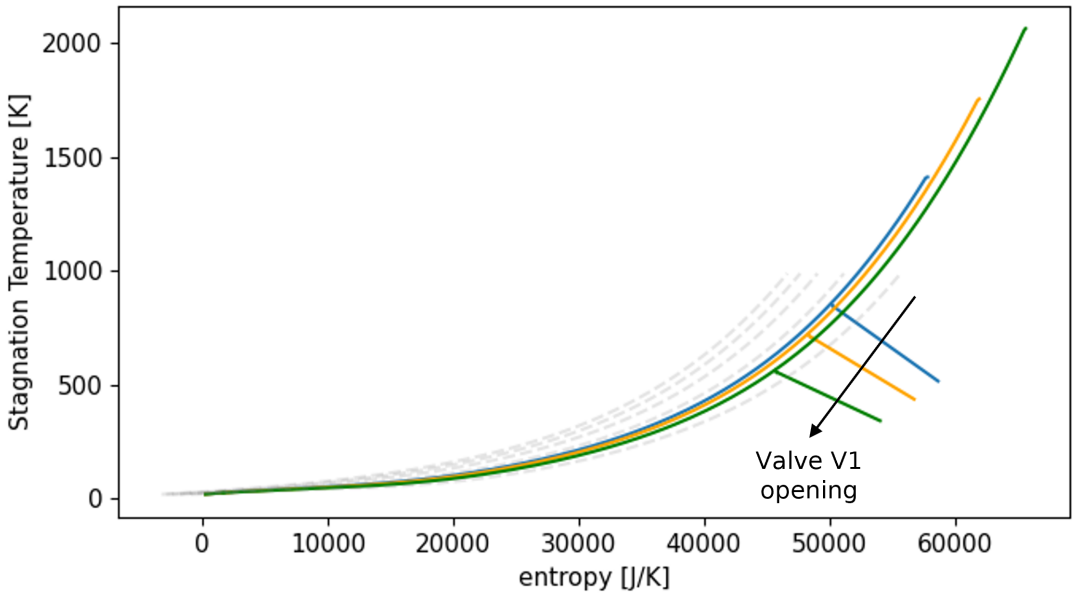

Figure 3.3: Heat capture control, cycle comparison, valve position: most closed (blue), mean position (orange), most opened (green).

Unlike Figure 3.2 where the transformations are recognizable, in this T-S chart the pump transformation, the hex pressure losses, and the turbine expansions are not distinguishable but still present. As shown in Figure 3.3, removing the heat source results in a smaller enthalpy jump available for the turbine. Intuitively, opening the valve lowers the stagnation temperature entering the turbine but simultaneously increases the temperature at the outlet of the heat exchanger (HEX). Deflecting the fuel flow implies less thermal capacity, resulting in higher temperatures even with a lower heat convective transfer coefficient. In this case, the fuel's cooling role is reduced. There is also a slight effect on the isobaric pressure inside the HEX, induced by the decreased pump head, as shown in Figure 3.3.

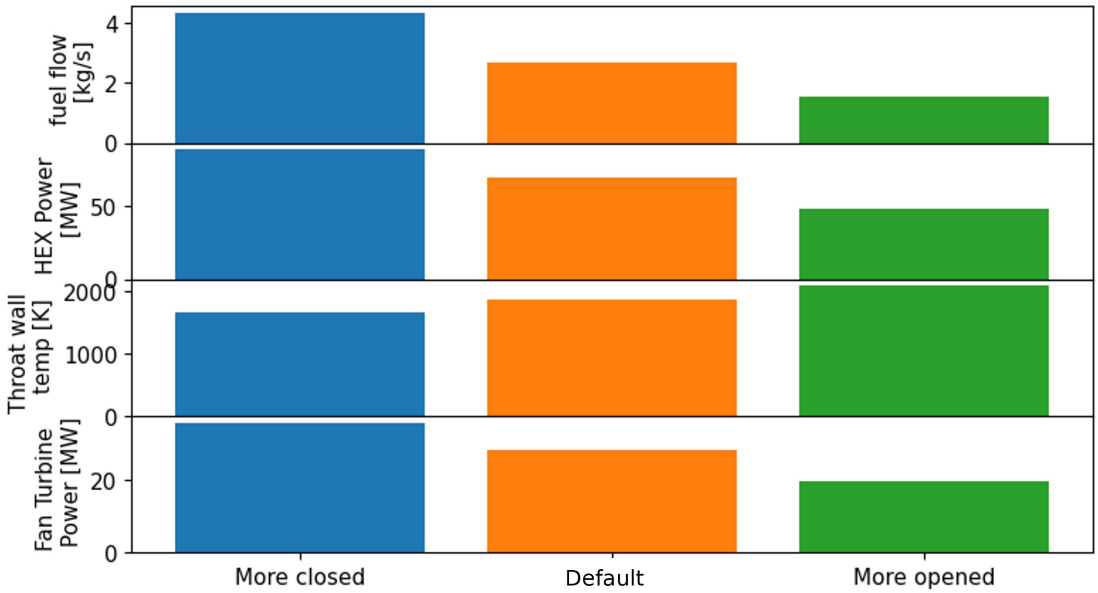

Figure 3.4: Heat capture control, fuel flow comparison, HEX power comparison, Throat wall temperature comparison, Fan Turbine power comparison.

The first row of Figure 3.4 shows how the valve opening induces a reduction in fuel flow, providing evidence for the earlier discussion and indicating a lower expansion of the pump turbine. The heat capture is reduced, as illustrated in the second row. Indeed, the wall temperature of the throat increases (third row), and the fan turbine power output decreases (fourth row). This control is effective in slowing down the spools.

3.2 In Line Control

The valve in series can be viewed as a change in the size of the fuel injector. Being in series with turbines, the valve shares the same mass flow rate. The valve introduces a pressure drop, altering the fuel circuit load pressure. Regarding the in line control, the opening of the valve allows for an increase in hydrogen flow, as shown in the first row of Figure 3.6. This can be explained by the momentum balance presented in equation 2.2.6 and illustrated in Figure 4.12.

In the equation discussed in section 2.2.6, the pressure loss source term depends on the valve area. A larger passage area (a more open valve) results in lower pressure losses, thus shifting the intersection with the pump head curve to a higher mass flow. Therefore, opening the valve increases the amount of hydrogen flow.

Focusing on Figure 3.6, when the valve is more closed, the stagnation temperature is the highest due to the lowest fuel flow, as shown in Figure 3.5. Opening the valve induces a higher working pressure inside the HEX. A slight entropy reduction is also visible. Dividing the fan turbine power by the HEX power provides a good approximation of the fuel circuit efficiency, as clearly seen in Figure 3.6. The green case shows the lowest hydrogen stagnation temperature at the HEX outlet, along with the highest heat pickup and the highest throat wall temperature. Compared to the heat capture control case, the variation in working pressure is more evident.

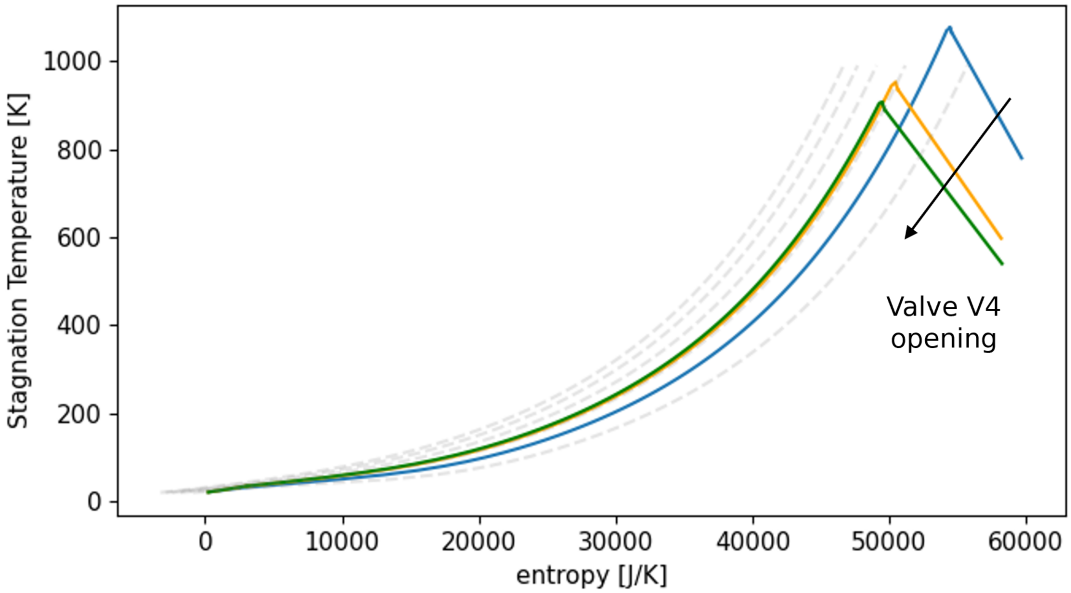

Figure 3.5: Injector size control, cycle comparison, valve position: most closed (blue), mean position (orange), most opened (green).

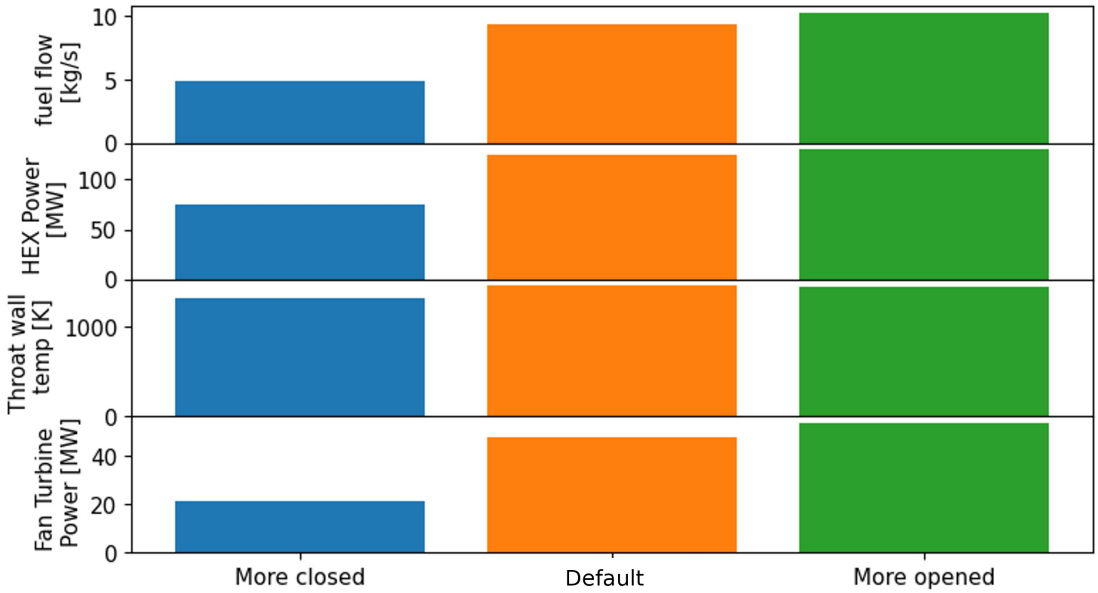

Figure 3.6: Injector size control, fuel flow comparison, HEX power comparison, Throat wall temperature comparison, Fan Turbine power comparison.

3.3 Pump Turbine Control

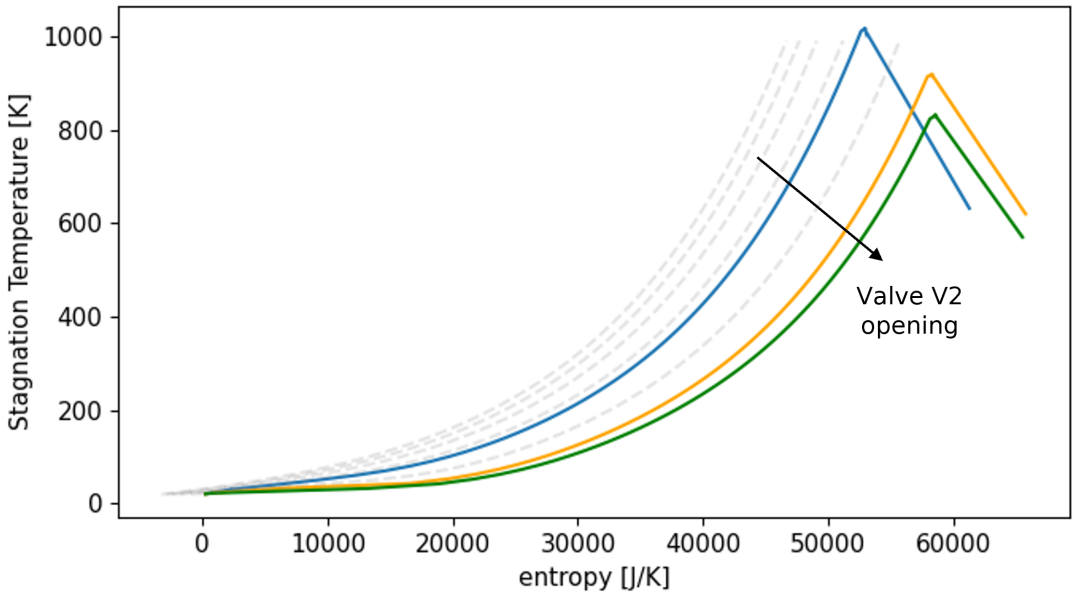

Figure 3.7: Pump Turbine Control, cycle comparison, valve position: most closed (blue), mean position (orange), most opened (green).

Figure 3.7 shows the strongest effect on the pressure inside the HEX. Similar to the injector case, the predominant movement occurs along the x-axis. In this scenario, the green cycle is not only the least efficient. It is operating at the lowest pressure and it reaches the lowest maximum temperature. The valve opening induces another effect, slowing down the spools. As shown in Figure 3.8, the fuel flow decreases, HEX Power reduction follows causing a smaller turbine expansion ratio and consequent limited power output. As an outcome, the throat wall temperature diminishes. In comparison with the Heat Capture Control, where the V1 valve opening increases the HEX outlet temperature, here the coolant role of the fuel is maintained. This control has an opposite behavior to the in line Control where the valve opening induces a spools speed up.

Figure 3.8: Pump Turbine Control, fuel flow comparison, HEX power comparison, Throat wall temperature comparison, Fan Turbine power comparison.

3.4 Fan Turbine Control

Figure 3.9 illustrates the effects of V3 valve opening. V3 is in parallel with the Fan turbine. The opening induces a flow deflection and expansion ratio reduction. In this case, the isobaric heat addition occurring inside the HEX seems unaffected, pressure wise. Thus, the opening of the valve slightly affects the pump turbine. Instead, the HEX outlet temperature is strongly influenced. As shown in Figure 3.10, the increased fuel flow improves the hydrogen heat capacity lowering the HEX outlet temperature, simultaneously the HEX power remains essentially constant. The higher fuel flow improves also the heat transfer coefficient.

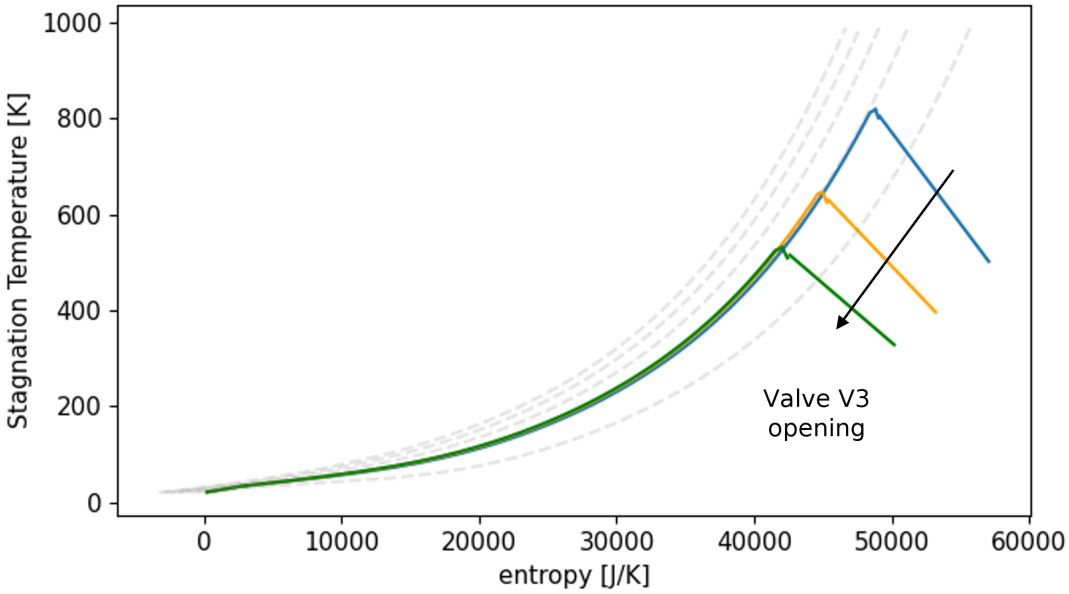

Figure 3.9: Fan Turbine control, cycle comparison, valve position: most closed (blue), mean position (orange), most opened (green).

The throat wall temperature decreases with valve opening. With the fan compressing less and the fuel flow increasing, the mixture ratio (MR) exceeds the stoichiometric ratio causing a lower combustion temperature thus a lower throat wall temperature. In the case with the more opened valve the MR is about 22 while the stoichiometric is about 34 [43]. A lower MR is a richer mixture, less kilograms of air are burned for one kilogram of fuel.

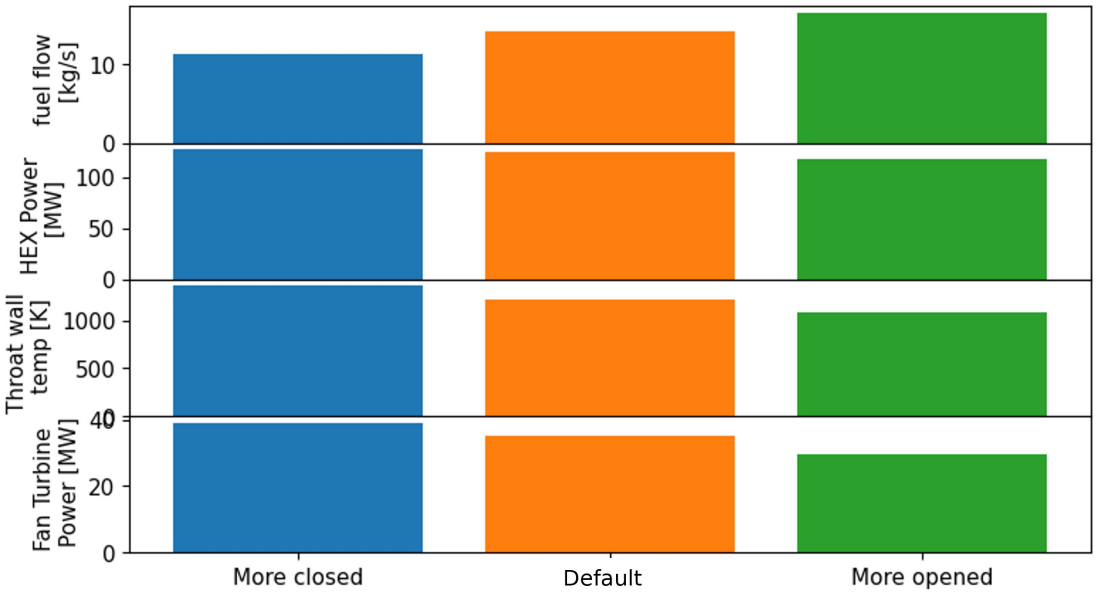

Figure 3.10: Fan Turbine control, fuel flow comparison, HEX power comparison, Throat wall temperature comparison, Fan Turbine power comparison.

3.5 Sensitivity Analysis

The opening and closing of a valve reflect on the entire system, highlighting the strong interaction between subsystems, the propulsive cycle, and the fuel-feeding system. In this section, all the previous controls are compared based on the changes in the mixture ratio (MR) and chamber pressure (P_c) induced by the valve opening, from the most closed position (blue case) to the most open position (green case). The analysis of controls is strongly affected by the starting conditions, such as flight conditions, how the analysis is conducted, and the system itself. Even though the perturbation imposed is a percentage of the initial position, the size of the valve still impacts the analysis. Moreover, the major changes are related to what happens inside the chamber in relation to the valve openings. The heat flow exchanged by the HEX depends on the chamber temperature, as demonstrated by the equations presented in section 2.2.8. Consequently, this also affects the turbines' expansion ratio. The fuel feeding system influences the propulsive system and vice versa. The injector size control is an example. The valve opening induces a higher fuel flow so the MR decreases while the fan turbine power output increases so the combustor pressure increases. Starting from a rich mixture as shown in Figure 3.5 approaching the stoichiometric, the combustor temperature increases leading to a higher heat capture by HEX. The starting condition is for all the same MR 37.3 P_c 136 kPa.

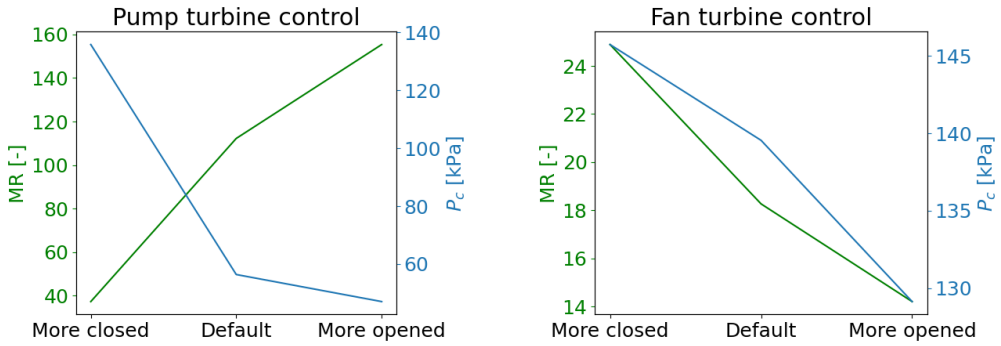

Figure 3.11: Effects on MR and P_c produced by fan turbine control (left) and pump turbine control (right) at different valve positions according to section 3.

Two trends are identifiable:

- MR and P_c have the same negative trend (Heat capture control, Fan Turbine control)
- MR and P_c have an opposite trend (Injector size control, Pump Turbine control)

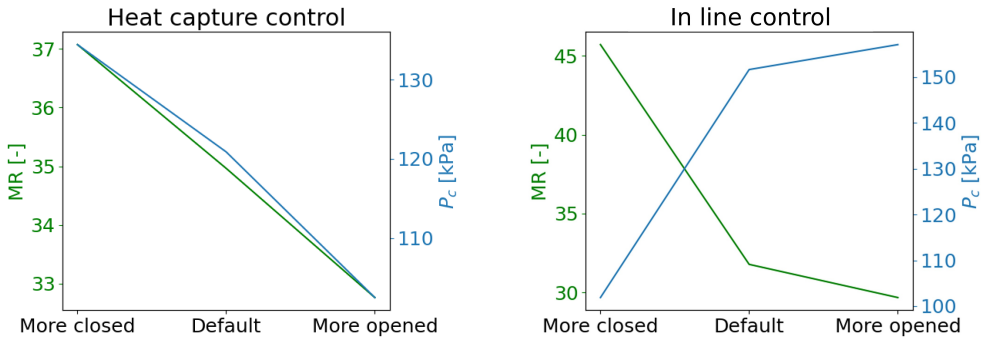

Figure 3.12: Effects on MR and P_c produced by heat capture control (left) and injector size control (right) at different valve positions according to 3.

It is now clear, how it is not possible to change one of the two throttle variables independently without affecting the other. Hence, to set both values the two valves have to compensate for their effects. Furthermore, two controls with opposite trends have to be selected. Such as the pump turbine and fan turbine control. To determine which combination of controls is more suitable, the table 3.13 is presented which summarizes figures and . To produce the table number the following formula has been used:

$$S_c = \frac{\frac{x(v+\Delta v)-x(v)}{x(v)}}{\frac{\Delta v}{v}} 100\%$$

with S_c being the sensitivity coefficient, x being the parameter to evaluate,v being the valve position between 0 and 1. So the percentual variation of the parameter is divided by the percentual variation of the valve position.

	MR			P_c		
	Valve opening →			Valve opening →		
	More closed	Default	More opened	More closed	Default	More opened
Heat Capture control		-6%	-6%		-11%	-12%
In line control	-45%	-29%	-13%	50%	23%	10%
Pump Turbine control		87%	106%		-25%	-22%
Fan Turbine control	-30%	-25%	-21%	7%	1%	-2%

Figure 3.13: Sensitivity table: percentual variation of MR and P_c respect valve positions according to 3.

From the blue case to the green one the respective valve of each control is more and more opened. The Pump control seems to be the most effective.

More closed	Starting values			Final values		
	P_c [Pa]	MR [-]	Valve Area [m^2]	P_c [Pa]	MR [-]	Valve Area [m^2]
Heat Capture control	1.36E+05	3.73E+01	5.81E-04	1.34E+05	3.71E+01	6.39E-04
Injector size control			3.96E-02	1.02E+05	4.57E+01	1.98E-02
Pump Turbine control			1.01E-03	1.36E+05	3.73E+01	1.01E-03
Fan Turbine control			3.35E-04	1.46E+05	2.49E+01	7.04E-04

Default	Starting values			Final values		
	P_c [Pa]	MR [-]	Valve Area [m^2]	P_c [Pa]	MR [-]	Valve Area [m^2]
Heat Capture control	1.36E+05	3.73E+01	5.81E-04	1.21E+05	3.50E+01	1.16E-03
Injector size control			3.96E-02	1.52E+05	3.18E+01	5.95E-02
Pump Turbine control			1.01E-03	5.64E+04	1.12E+02	3.32E-03
Fan Turbine control			3.35E-04	1.40E+05	1.83E+01	1.01E-03

More opened	Starting values			Final values		
	P_c [Pa]	MR [-]	Valve Area [m^2]	P_c [Pa]	MR [-]	Valve Area [m^2]
Heat Capture control	1.36E+05	3.73E+01	5.81E-04	1.02E+05	3.28E+01	1.74E-03
Injector size control			3.96E-02	1.57E+05	2.97E+01	1.00E-01
Pump Turbine control			1.01E-03	4.70E+04	1.55E+02	4.02E-03
Fan Turbine control			3.35E-04	1.29E+05	1.42E+01	1.34E-03

Figure 3.14: Sensitivity table: row data.

Chapter 4

Control System

In Figure 3.1 it is shown where the valve can be placed. Each valve is a system degree of freedom. Hence, to control MR and P_c, two valves are needed. Theoretically, it is thinkable to use any valve to control MR or P_c. Practically, some engine stations are more sensitive to the control, making them more effective at changing engine performance.

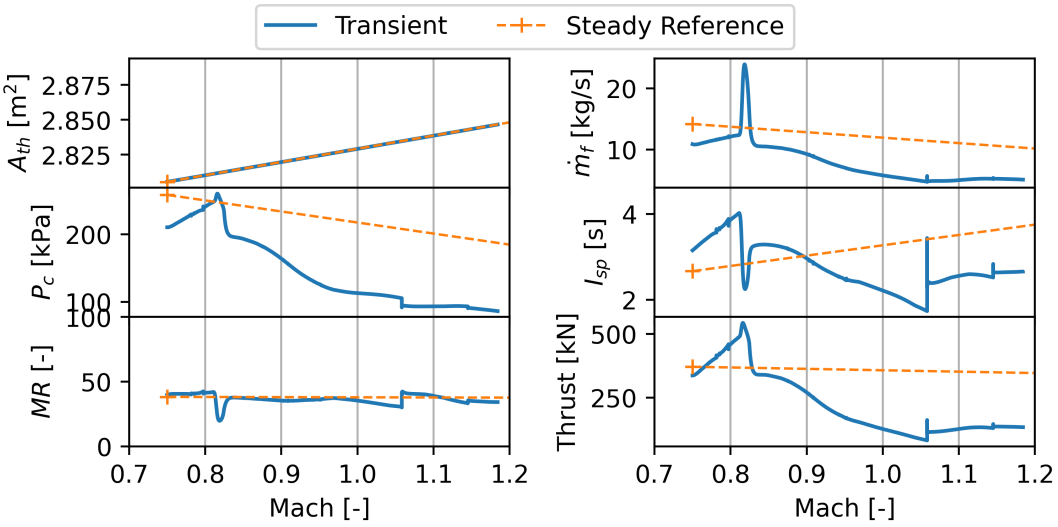

Figure 4.1: Ineffective control strategy.

For instance, it has been tried to modify MR with V1 and P_c with V3. Changing the heat addition involves a different enthalpy jump on the pump turbine, inducing a variation in hydrogen mass flow rate, thus resulting in a new MR. Instead, more air introduced into the chamber will increase P_c. At least, this is what logic would say. The variation of heat capture to reach the MR is so severe that the fan

turbine is no longer able to provide enough energy to the fan, as shown in Figure 4.1. Different combinations have been tried with the same result. The only one that worked was the bypass on the pump turbine controlling MR. The control strategies that are actually capable of following the set signals are:

- Injectors variable size. V4 controls P_c. (CS3)
- HEX bypass. V1 controls P_c. (CS2)
- Turbines bypass. V2 controls P_c. (CS1)

The best control system ensures as much as possible controllability range for MR and P_c with the lowest cross-coupling effects between actuators. Therefore, what makes a good control system is the valve combination that allows, as much as possible, the decoupling of turbines. In fact, to achieve the most extensive range of MR and P_c combinations, perfect decoupling is desirable—that is, having a valve that impacts only MR or only P_c, as seen in section 3.5. However, this is not what happens within this engine. Figure 4.2 shows the chosen control system: the pump turbine bypass (V2) is implemented to control MR, while the fan turbine bypass is used to control P_c.

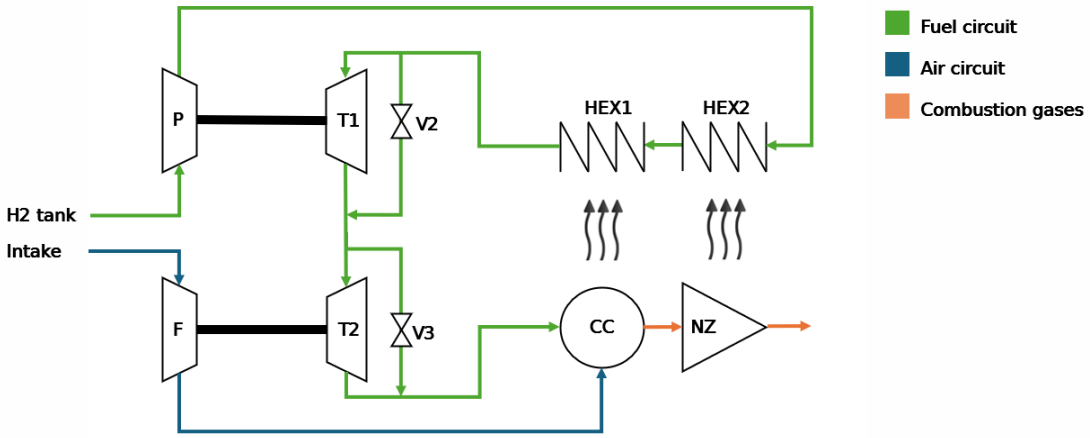

Figure 4.2: Engine scheme with chosen actuators.

To explore the limits of throttling MR and P_c different experiments have been conducted. The A_{th} is kept constant to highlight the effect of the other two throttle variables. MR and P_c are inversely proportional to A_{th}. For Mach 0.75, MR is kept constant while P_c decreases as shown in Figure 4.3. The MR control is not actually able to follow the signal.

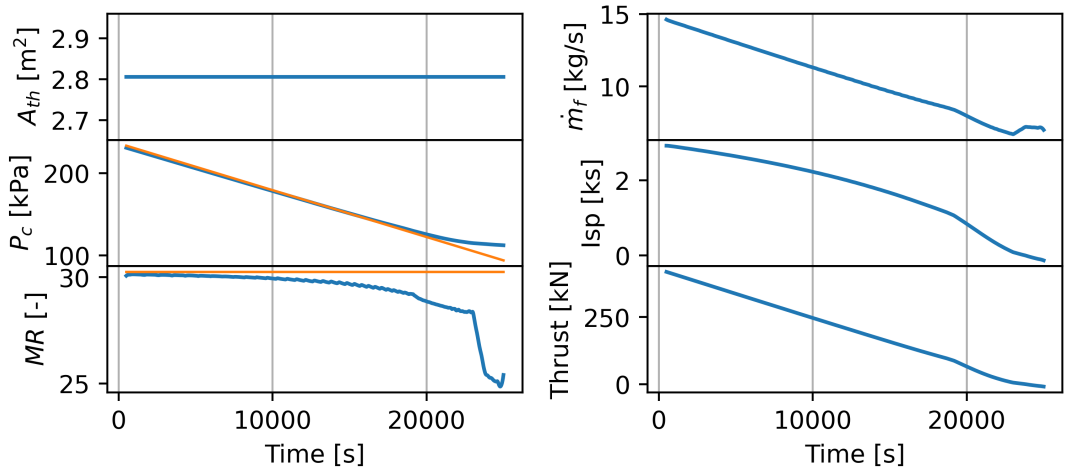

Figure 4.3: Throttle experiment 1, constant MR and decreasing P_c.

As shown in Figure 4.4, to decrease the P_c, V3 will open decreasing the power delivered to the fan causing lower compression ratio and air flow. The shaft slows down. From section 3.5 V3 opening results in a decreasing MR to compensate this effect V2 also opens.

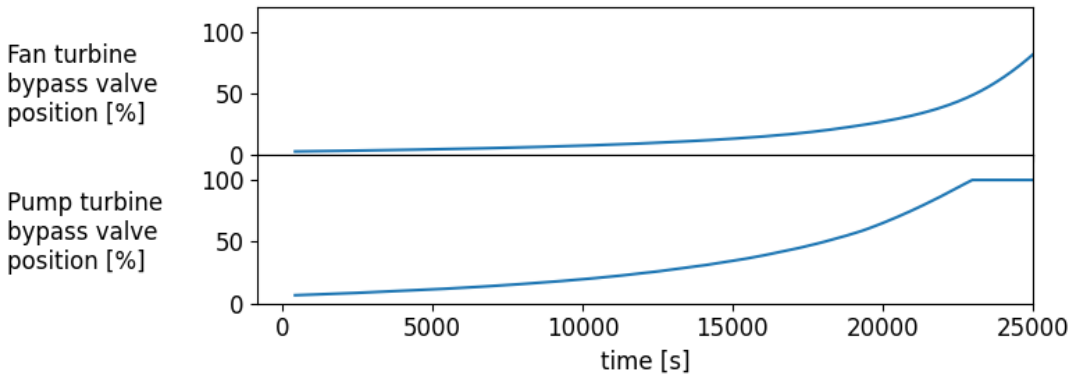

Figure 4.4: Throttle experiment 1, valves position over time.

As shown in Figure 4.5 the spool keeps slowing down until there is not enough energy in the system that the turbine can extract to power the fan. This simulation indicates that it is not possible to maintain the same MR for all P_c values, and lowering P_c results in a slowdown of the engine as shown in Figure 4.6. Within the control strategy, there is a limit on throttle range. In the second experiment,

both MR and P_c are imposed to increase. To achieve this, the controllers will close the valves. This attempt is the opposite of the previous one; in this case, the engine is speeding up. Valves V2 and V3 close simultaneously. Increasing P_c means increasing the airflow; clearly, the imposed MR is lower than the MR without control, so V3 closes as well. After that, the system is unable to speed up any further. The closure of V2 causes a discontinuity. Valves and turbines can be viewed as resistors in parallel; the equivalent resistance will be lower than the lowest individual resistance. When the valve is completely closed, the pressure drop increases, causing a lower power extraction.

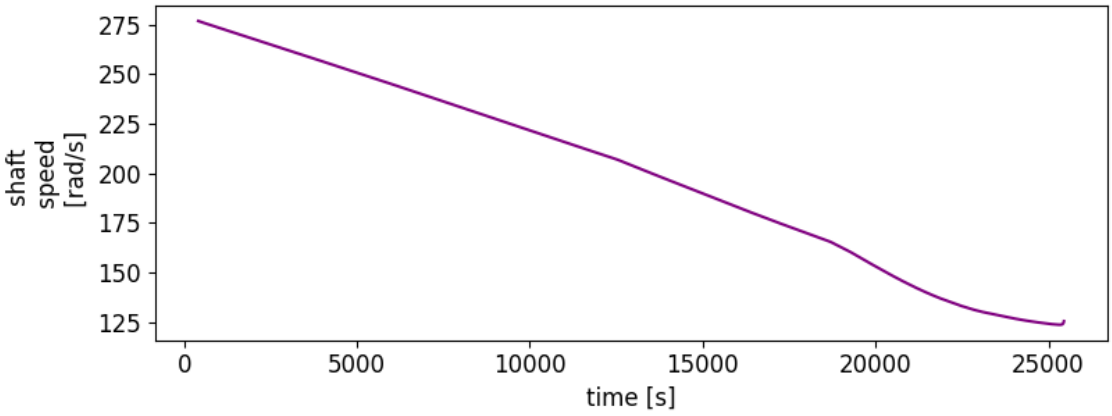

Figure 4.5: Throttle experiment 1, fan shaft speed over time.

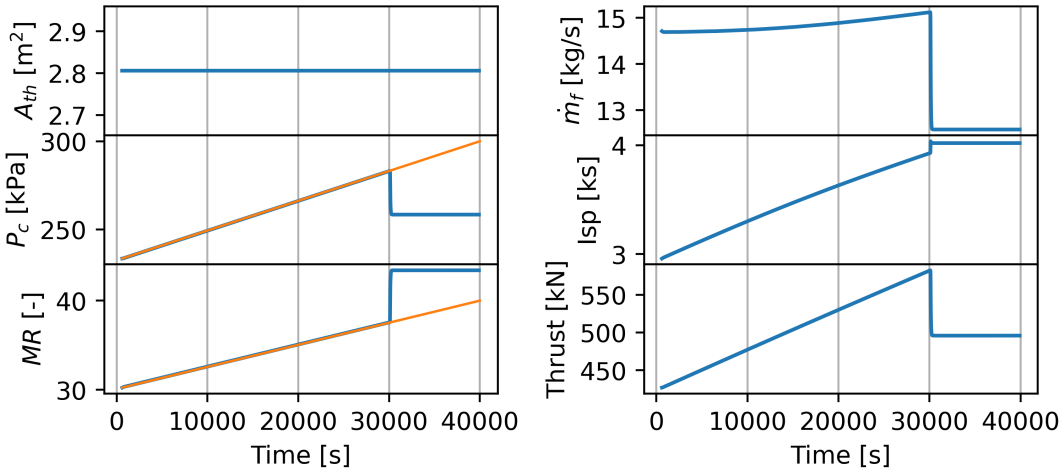

Figure 4.6: Throttle experiment 2, increasing MR and P_c.

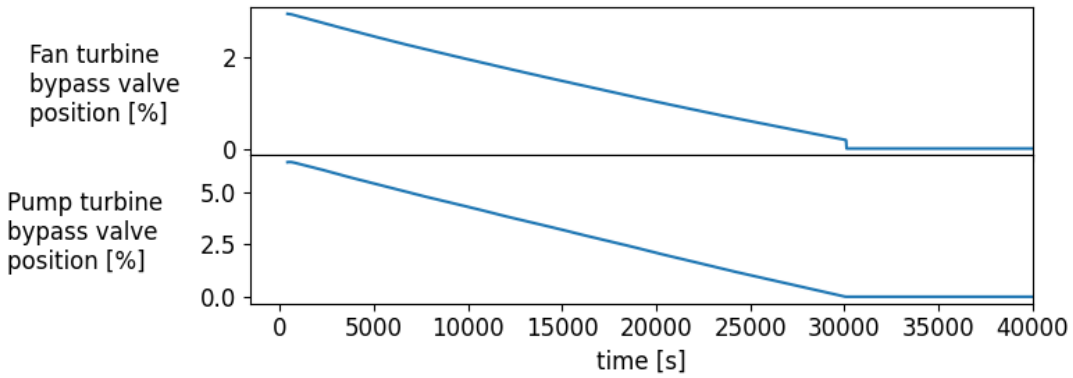

Figure 4.7: Throttle experiment 2, valve position over time.

Also in this case, it is not feasible to set MR and P_c independently, but there is a range where both valves can be fully open or fully closed. A_{th} could increase the controllability range, as it lowers the mass flow rate for example. Focusing on the last 2000 seconds of Figure 4.6, the valves are completely closed. The flight conditions and tank conditions remain constant, as does the system response. For some operating conditions and throttle parameter settings, there isn't sufficient controllability range, even with fully closed valves, as there simply is not enough energy in the hydrogen loop to be extracted.

4.1 Control System Stability

A stable control system is one in which the output remains bounded and does not exhibit uncontrolled or oscillatory behavior, even when subjected to external forces or variations in input. Three points along the ascend trajectory have been replicated which will be discussed in more detail in section 4.4. For each point, a certain period of time is observed to assess how the control system reacts. The signals in Figure 4.8 between 0 and 1000 seconds, 10000 and 12000 seconds, 20000 and 22000 seconds are constant lines. Consequently, the control system is stable under those flight conditions. Additionally, 4.9 shows the valve behavior as further proof of stability; in fact, the valve opening remains constant.

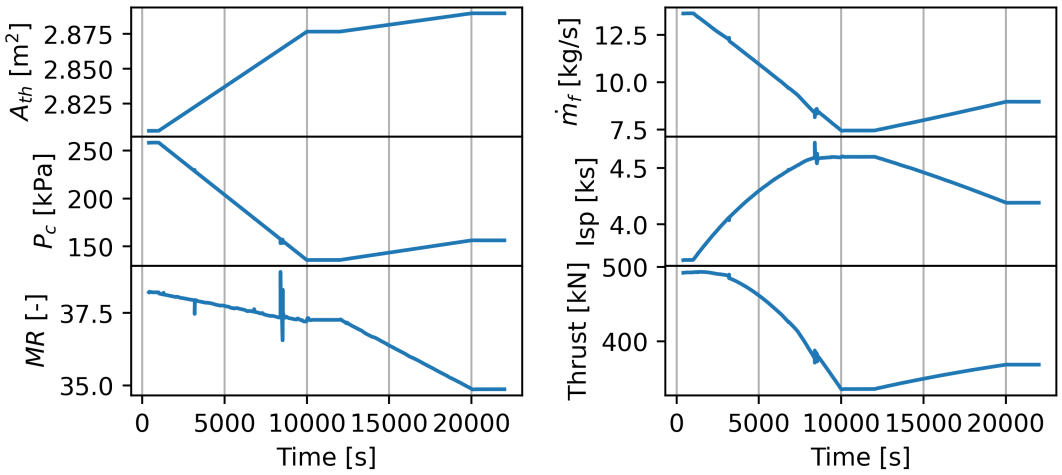

Figure 4.8: Steady state at Mach 0.75-1.5-2,throttle variables and $\dot{m}_f$, I_{sp}, thrust over time.

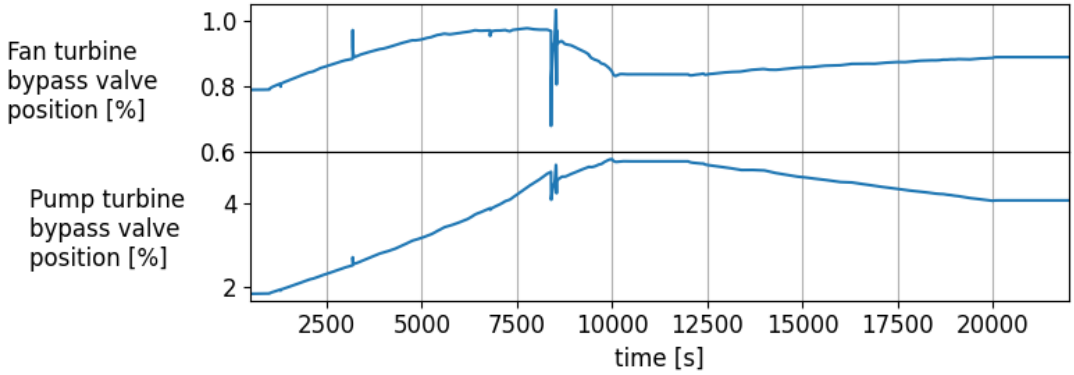

Figure 4.9: Steady state at Mach 0.75-1.5-2, valves position.

To prove stability a transfer function analysis should be conducted. For a linear time-invariant system, this is possible. For a non-linear MIMO system like this engine is not possible to pursue this path. Some speculations can be made to explain this stability behavior. First of all, the pressure drop across the heat exchanger is a quadratic function of the mass flow rate, while the heat capture is shown to be linear. Thus, moving away from the optimal point results in a less convenient trade-off 4.10. In the figure, the percentage variation is shown with respect to the mean value along the ascent trajectory.

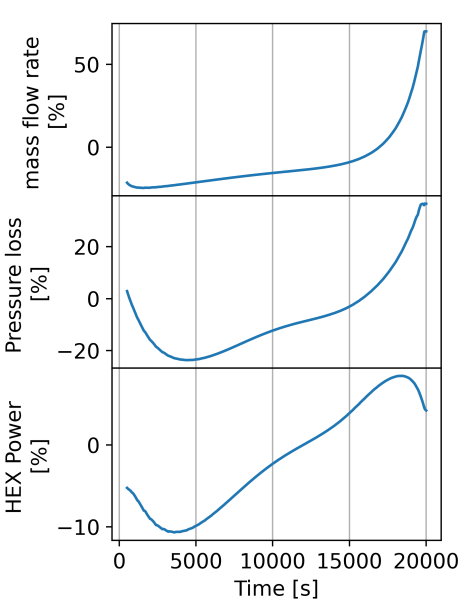

Figure 4.10: Trajectory, percentual variation of HEX pressure losses, HEX Power, fuel mass flow.

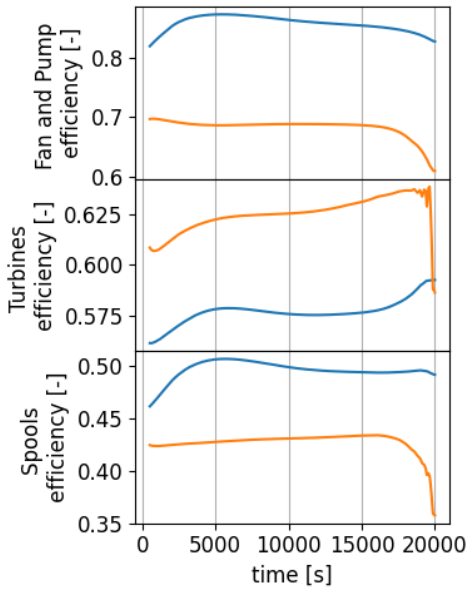

Figure 4.11: Fan,fan turbine, fan spool efficiencies (blue), pump, pump turbine, pump spool efficiencies (orange).

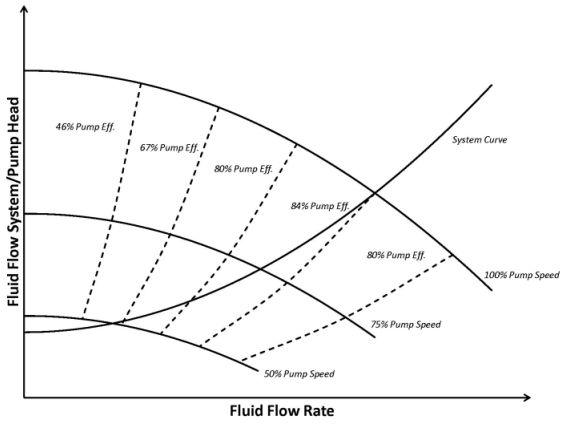

Figure 4.12: Sketch of Head pump and system load vs volume flow rate [10].

Second, the consequence of higher energy availability is the possibility for the turbines to spin faster thus the compressor will increase the P_c, thus limiting the turbine's pressure jump. In the chamber, both fuel and air have the same pressure. So to avoid counter flow, the pressure at the inlet of injectors has to

be higher. The turbine expansion ratio is limited. Another reason is the turbo machinery efficiency drop moving off the optimal point.4.11 Further explanation reveals that the pump map illustrates how, at higher volume flow rates, the system load increases rapidly, while the pump head decreases. Beyond a certain value, it becomes impossible to increase the mass flow rate. This represents another negative feedback loop, resulting in an upper limit for the system, specifically a maximum shaft speed. Additionally, there is a minimum heat capture required to keep the engine operational.

4.2 Step Response

The resulting accuracy of the following experiment is strongly affected by the model limitations described in section 2.5.1. To better represent the factual reality, an accurate fluid and spool inertia have to be estimated and a more sophisticated intake model introduced. Within this limitation, the turbomachinery behavior described should still be realistic but the time frame and exact values could change.

The experiment consists, at fixed flight conditions Mach 0.75, a throttling up, and a throttling down. Imposing directly the throttle variables (P_c, MR, A_t) it has been possible to increase F_u from $350kN$ to $375kN$ and back to starting value as shown in Figure 4.13.

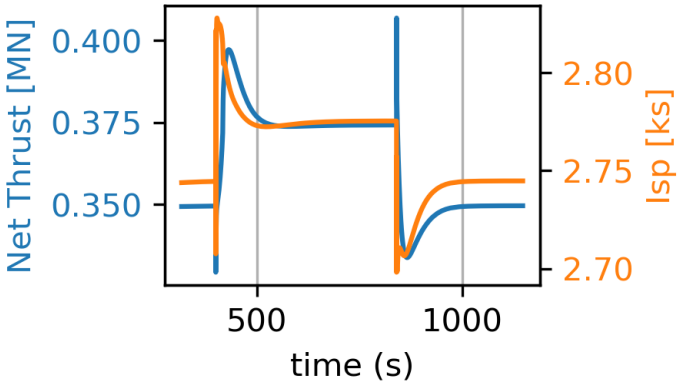

Figure 4.13: Step response of the thrust output and specific impulse.

In Figure 4.14 the orange lines refer to the set signals the blue the controllers response.

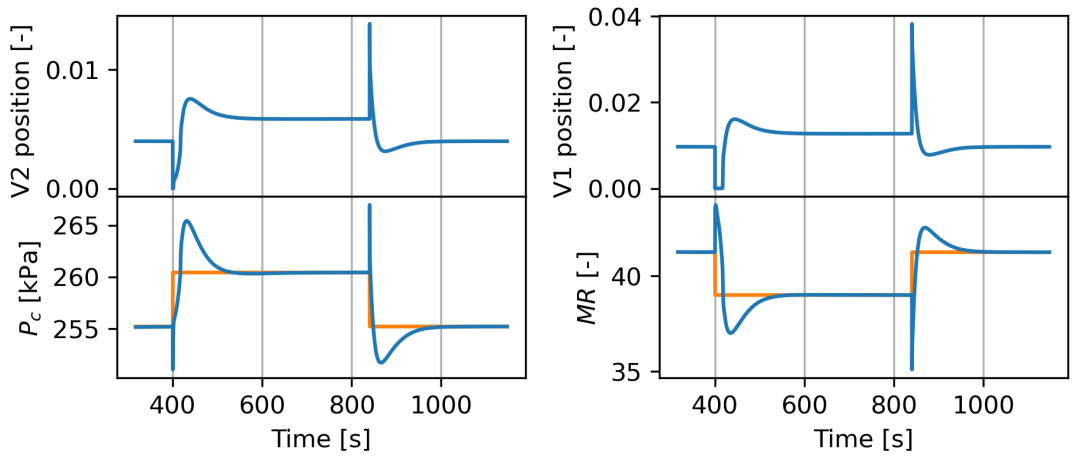

Figure 4.14: The bottom plots show the response of the engine throttle parameters (blue) for a step input (orange). The top plots show the response of the control valves.

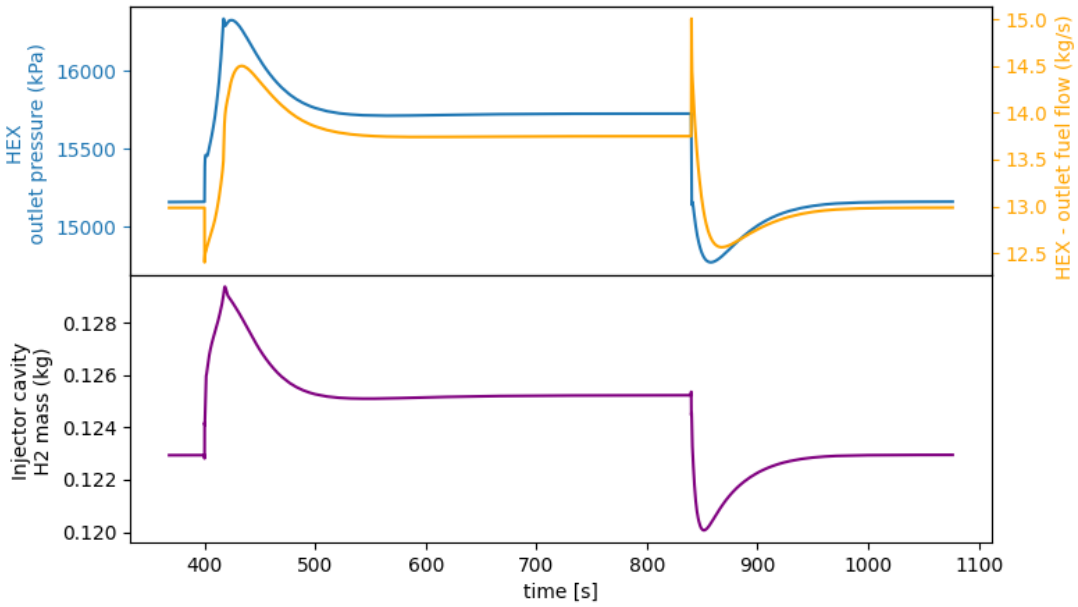

Figure 4.15: Step response, first row shows HEX outlet pressure (blue) and HEX outlet fuel flow (orange) over time. Second row shows H2 mass inside fuel injector cavity over time.

Instantly valves close almost completely. A pressure wave reaches the HEX outlet with a consequent mass flow drop at the same time the hydrogen mass inside the injectors increases. This explains the smaller spikes at 400 s shown in Figure 4.15. As a result, less fuel is reaching the chamber thus the Pc drop and the MR rise as illustrated in Figure 4.14.

The fuel flow is forced to pass through the turbine thus the flow resistance across the turbine-valve system increases. As shown in Figure 4.17 the turbomachinery pressure fields quickly adjust to the new conditions, way faster than the mass flow penalized by the fluid and spool inertias. This is particularly evident on the map of Turbine 2 (Fan turbine). When the step-up occurs, the pressure rapidly adjusts to the new conditions, resulting in a sharp increase in the pressure ratio. This is observed as an upward shift of the operating point, parallel to the black constant speed lines. The increased pressure ratio boosts the power available in the spool, causing it to accelerate, which is indicated by the operating point shifting to the right, towards higher constant speed lines. Shortly after, the valves open again to counteract the overshoot of P_c and MR reaching the set signals without steady-state errors.

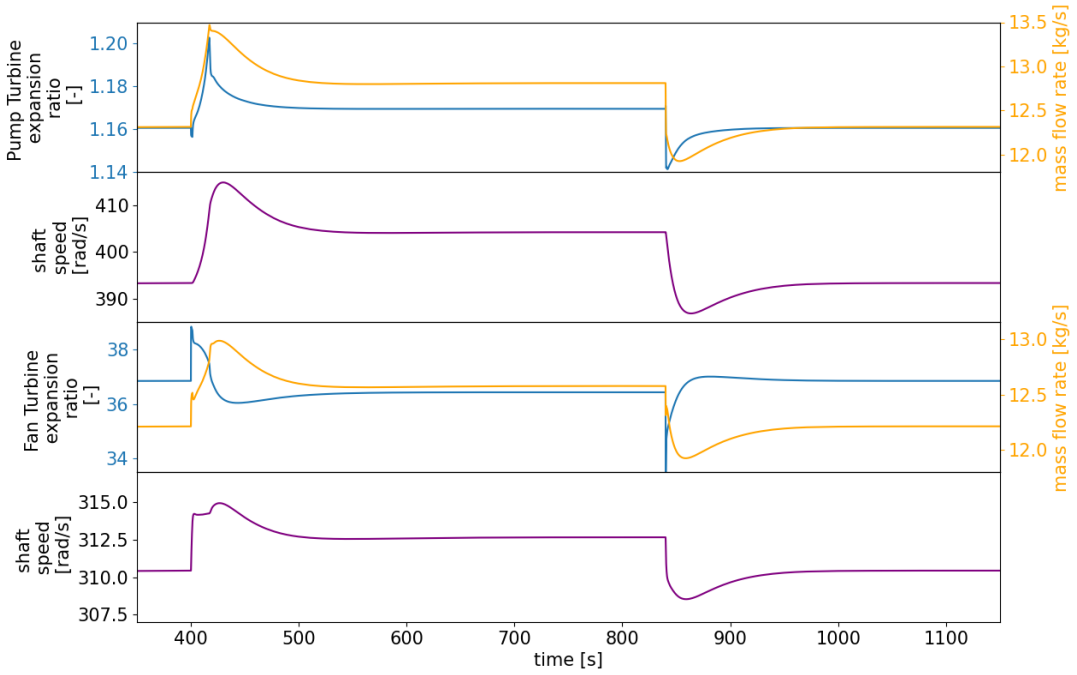

Figure 4.16: Step response, first row shows Pump expansion ratio (blue) and fuel flow passing through(orange). Second row shows pump shaft speed. Third row show Fan expansion ratio (blue) and fuel flow passing through(orange). Fourth row shows fan shaft speed.

This turbomachinery behavior is visible also on their map making it clear the hysteresis cycle. What happens during the down-throttle step is similar but in the opposite sequence during the up-throttle phase. The PI gain values are particularly important in this case because based on that the valves will open with possible jeopardy of let shut-down the engine if the closing period after the overshoot is not quick enough.

It is also interesting to note that, in contrast to conventional turbojet engines, an upward thrust step is beneficial to the compressor stall margin, while a downward step is detrimental.

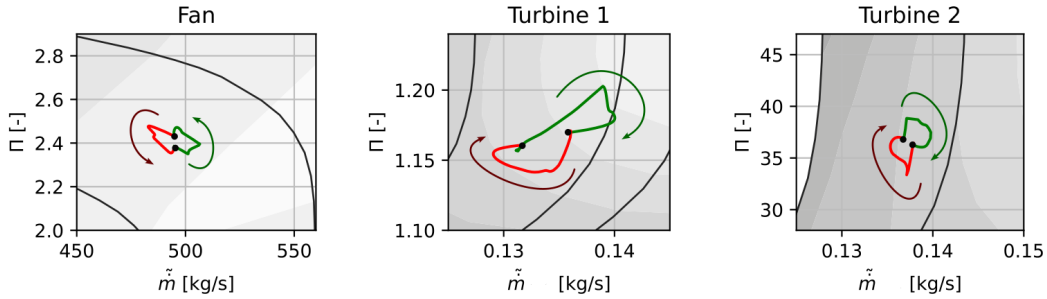

Figure 4.17: Locus of the turbomachinery operating points for the step experiment. The green curve indicates the up-throttle step and the red curve the down-throttle step.

4.3 Throttle Curve

Figure 4.18 summarizes the results of the steady-state optimization. At Mach 0.75, all individuals are displayed and compared based on thrust and fuel consumption. Each individual represents an engine at the same time and can be viewed as a throttle setting for a single engine under the same flight conditions. The Pareto front can be interpreted as a throttle curve. Each individual is a unique combination of

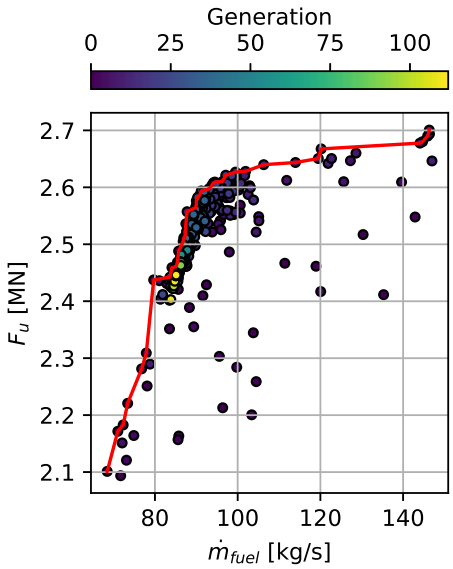

Figure 4.18: All explored points during the cycle optimisation at Mach 0.75. The Pareto-front is indicated in red.

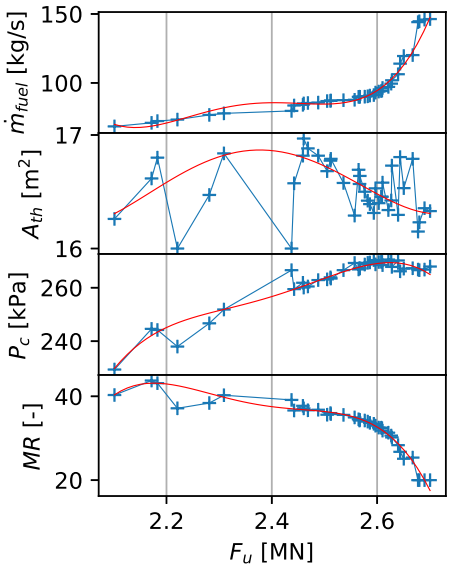

Figure 4.19: Evolution of the throttle variables along the Pareto front. Red shows a polynomial regression of order 4.

P_c, MR, and A_t. In Figure 4.19, the variables of the Pareto front individuals are shown. The curves from 4.19 are replicated in the transient model following the polynomial regression of order 4 (red line in Figure 4.19). To reduce control lag, the experiment is conducted over a simulated period of 20,000 seconds, allowing the engine to operate in a quasi-steady state.

Figure 4.20 compares engine performance and the throttle variables for the steady and transient models. The control system can set the throttle parameters to the required values effectively. It differs from the on-design performance, which is not unexpected given how much ultimately the system has been altered. The nozzle from being one for the whole propulsion plant in the steady-state simulation, is resized for just one ATR. Consequently, the HEX design changed to meet the new

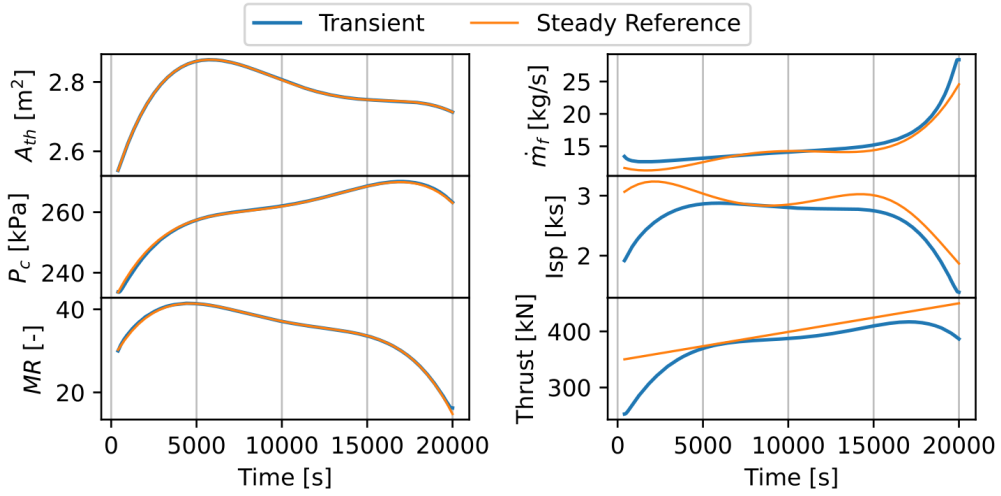

Figure 4.20: Throttle curve, throttle variables and $\dot{m}_f$, I_{sp}, thrust over time.

requirements in terms of size and power dissipation. In the steady state analysis, only the power balance between turbomachinery was considered, instead in the transient one the speed matching is also performed. The transient turbomachinery model is more realistic, taking into account the turbomachinery map, with respect to the steady one where the efficiency was constant independently of the operating point. These results mainly show that while the methodology that was outlined can be used, it differs too much from the steady model. Hence, it is necessary to perform an optimization like the one performed for the steady model, but for the transient one, to take all these changes into account. Looking at equation 4.1, A_{th} and P_{th} are imposed, resulting in the best match for fuel flow.

$$\dot{m} = \frac{A_{th} P_{th}^0}{\sqrt{R_{gas} T_{th}^0}} f(M = 1) \tag{4.1}$$

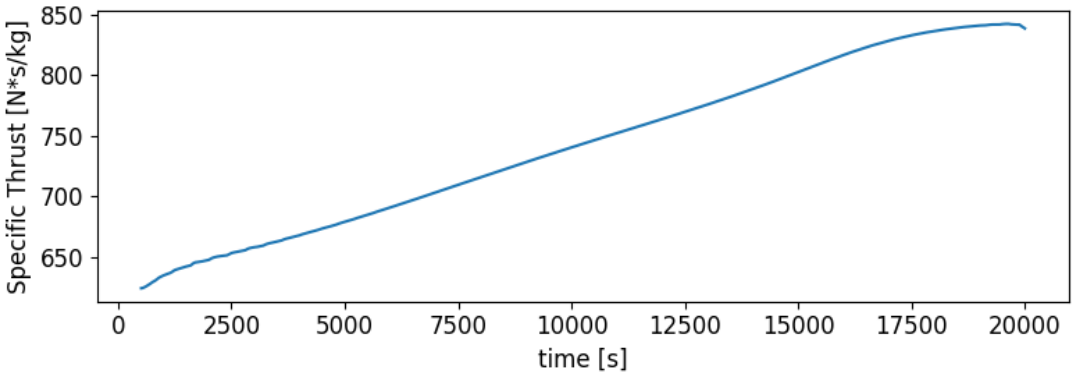

Figure 4.21: Throttle Curve, specific thrust over time.

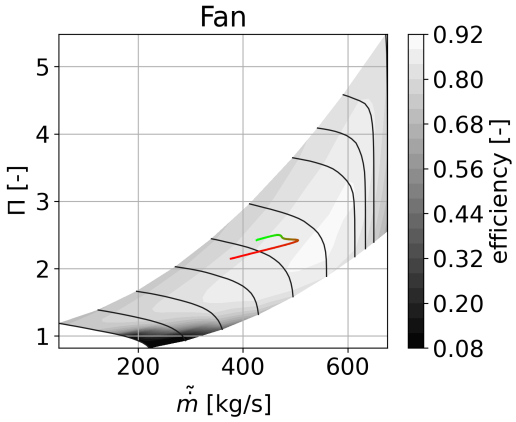

Figure 4.22: locus of fan operating point during ascend trajectory. The color goes from red to green as time progresses.

Figure 4.21 illustrates how burning at lower MR induces a lower specific impulse, but at the same time results in a higher specific thrust. These two figures of merit measure different aspects: the first indicates how efficiently the fuel is used, while the second measures the engine's capability to accelerate the air. It is now evident that a richer fuel mixture leads to a higher specific thrust, but also to a lower specific impulse. Figures 4.22, 4.23, 4.24 show the turbomachinery operating points. The color of the locus indicates the time of the simulation, with red representing the start of the simulation and green representing the end. It was not possible to keep all the working points on the maps during throttling. For the Fan turbine, there are two small excursions towards both the high and low ends of the throttle curve, the limiting factor seems to be the corrected mass flow rate range. For

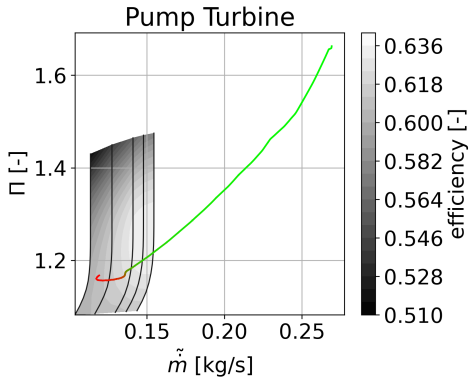

Figure 4.23: locus of pump turbine operating point during ascend trajectory. The color goes from red to green as time progresses.

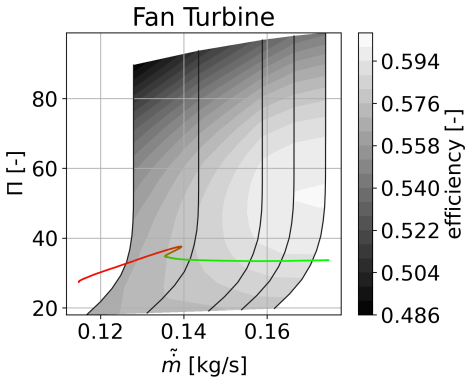

Figure 4.24: locus of fan turbine operating point during ascend trajectory. The color goes from red to green as time progresses.

the pump turbine, a large excursion is found at high throttle settings towards the high corrected mass flow range. The expansion ratio also exceeds the limit of the map, although this could realistically be resolved by adjusting the scaling. For the Fan, the operating point lies well within the boundaries of the map. To ensure wider operability of the turbines, the scaling procedure can no longer be used, as this methodology is unable to extend the range for both high and low mass flow rates. Either another scaling needs to be implemented, or maps of more representative machines need to be sourced. Furthermore, this behavior indicates how the turbomachinery limits the throttle range.

4.4 Ascend Trajectory

Due to a lack of simulation convergence, only the trajectory from Mach 0.75 to Mach 3 is simulated, as presented in 1.3. For each flight condition, the controllers receive a value for each throttle variable as set signals. The reasons for the divergence are still to be identified. The points of major interest are at Mach 0.75 and 1691 m altitude, Mach 1.5 and 14102 m, and Mach 2 and 15871 m.

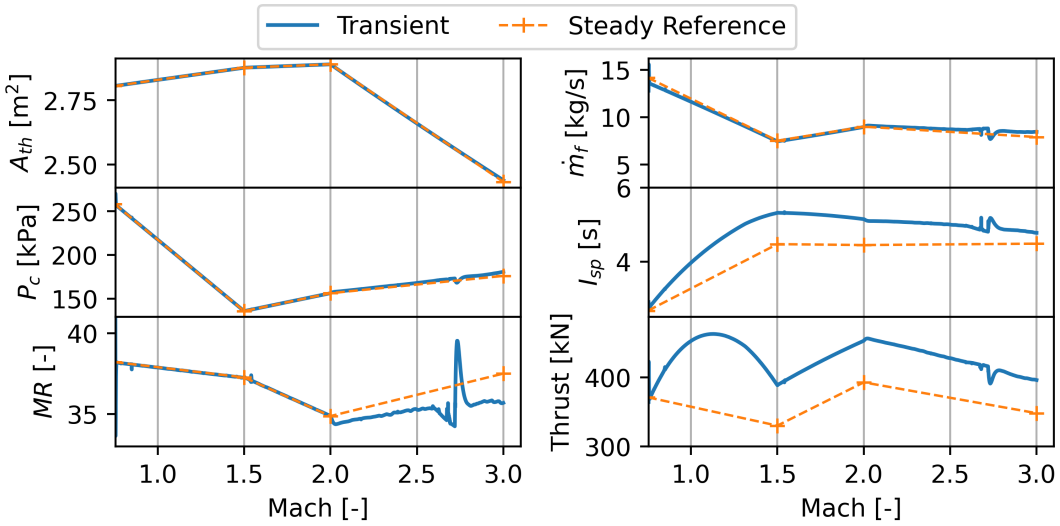

Figure 4.25: Trajectory until Mach 3, throttle variables and $\dot{m}_f$, I_{sp}, thrust over time.

The simulation starts from Mach 0.75 and progresses to Mach 3, with a simulated time of 60,000 seconds to avoid overshoots and complications related to PI tuning. Furthermore, the analysis can be considered as a quasi-steady state. It is not expected a linear behavior of the engine performance. In fact, in between the points, the behavior is unknown a priori. The controllers can follow the set signals up to Mach 2 see Figure 4.25. To reach Mach 3, the time between the two steady states has been reduced until the simulation converges. Interestingly, the transient model shows I_{sp}, and thrust values are above the references for the entire trajectory. The fuel flow and P_c are well matched, but MR is not above Mach 2. The not-matching seems to be more related to the control than the engine in itself. A MR spike can be noticed over the requested value. Additionally, there is a noticeable wavering in the MR signal, indicating that the control system is struggling to match the requested throttle values and is not functioning stably. Also the turbomachinery, even after the scaling procedure, is not compliant. With respect to the throttle curve experiment, there is an even bigger excursion which can be noted on the

turbine maps. For the Fan, the pressure ratio is moving towards unity, showing the engine is starting to behave more like a ramjet than an ATR-EXP as illustrated in Figure 4.26. In the sense that, the intake dynamic compression is already sufficient to fulfill the P_c request. This however leads to behavior that is numerically difficult to resolve.

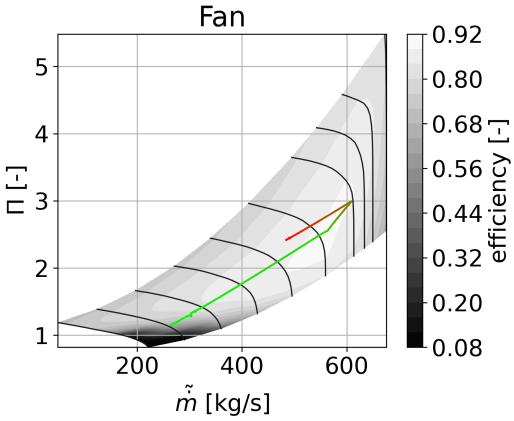

Figure 4.26: locus of fan operating point during ascend trajectory. The color goes from red to green as time progresses.

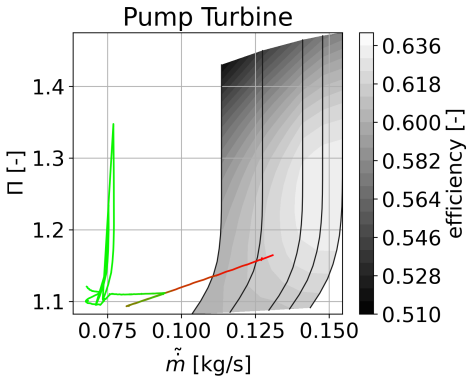

Figure 4.27: locus of pump turbine operating point during ascend trajectory. The color goes from red to green as time progresses.

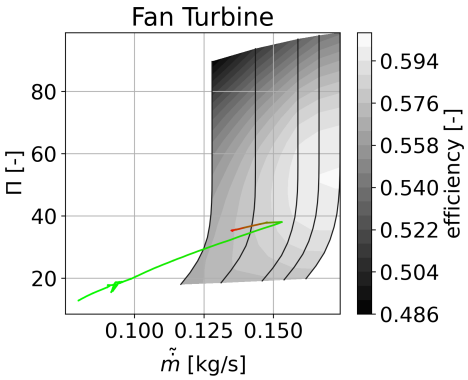

Figure 4.28: locus of fan turbine operating point during ascend trajectory. The color goes from red to green as time progresses.

The Sankey diagrams illustrate the relative magnitude of energy flows throughout the engine. The pump power is an order of magnitude smaller than the fan power,

resulting in the expansion ratio of the pump turbine being a tenth that of the fan turbine as shown in Figure 4.29 and Figure 4.30. Additionally, the energy used by the fuel line is modest compared to the total energy released during the combustion process. This is primarily due to the heat capture rate being constrained by the heat exchanger technology and weight, which limits the fan compression.

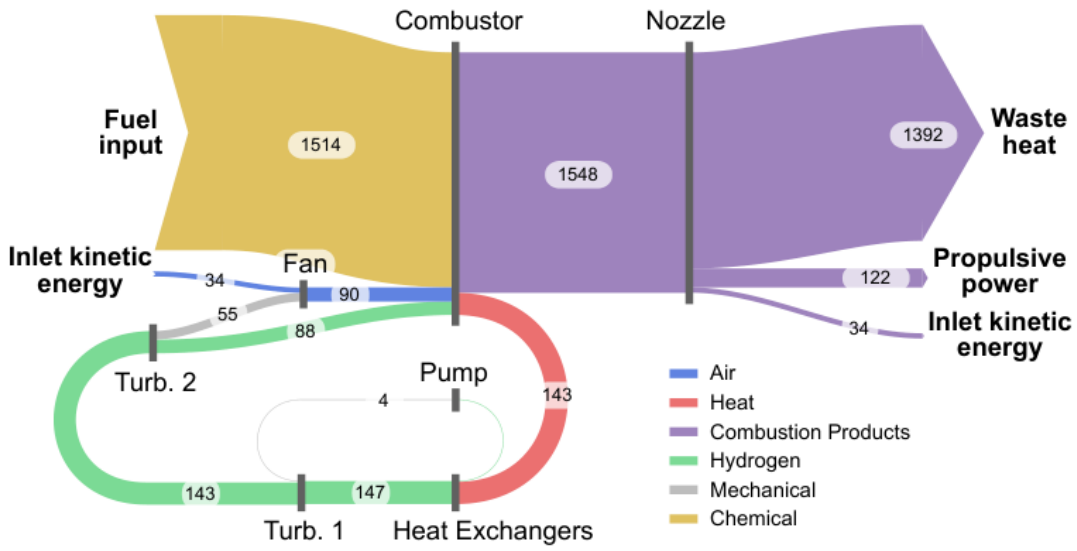

Figure 4.29: Sankey diagram showing the power flow in kW for Mach 0.75.

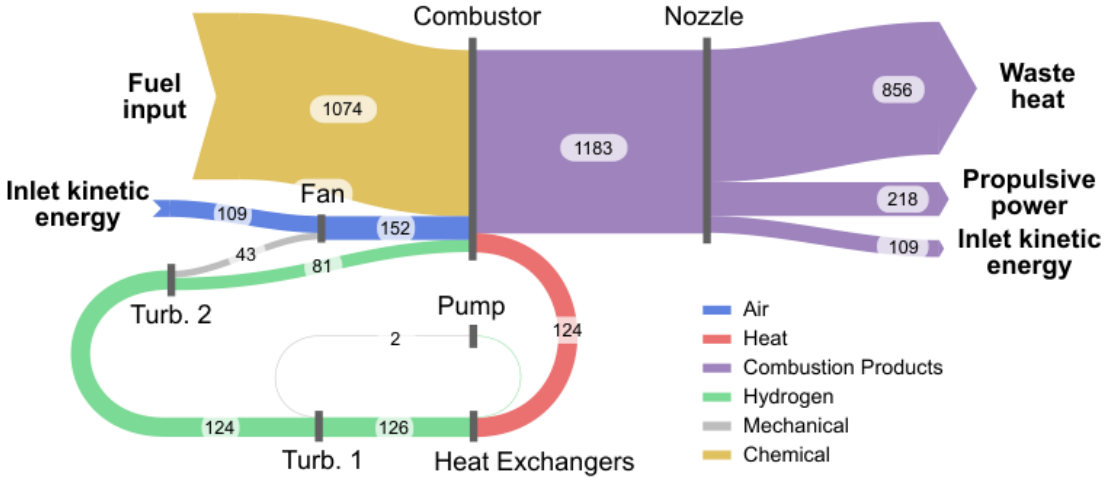

Figure 4.30: Sankey diagram showing the power flow in kW for Mach 2.

Conclusions

A mathematical formulation to define the ATR cycle has been proposed for steady-state conditions. This model suggested that the system can have three degrees of freedom or throttle variables. The chosen ones are combustion chamber pressure, mixture ratio, and throat area. The chamber pressure has a major impact on the performance of the fuel feeding system, which itself forms a Rankine cycle. The mixture ratio is strongly linked with fuel consumption. The throat area scales the net thrust output by controlling the air mass flow rate admitted by the engine.

These throttle variables are controlled by several valves, also called control actuators, which can be placed in series or parallel with respect to the turbines and heat exchanger. Four possibilities for actuators have been compared in terms of their effect on the throttle variables and other critical engine state variables. A large cross-coupling was noted, with each actuator having a large effect on all throttle variables. The four controls proposed are:

- Heat capture control, able to modify the heat exchanger working point,
- In line control, the usual solution for controlling the fuel flow,
- Pump Turbine control, alternative solution to shift the turbopump working point,
- Fan Turbine control, an option to control the fan working point.

The present work has been able to develop a control system based on the control strategies described through the implementation of PI controllers. The control system has been proven to be capable of tracking the imposed control variables in different numerical experiments such as step response, ascend trajectory, and so-called, throttle curve experiment. Strong cross-coupling phenomena have been noticed. The intended controller influences not only the interested throttle variable but also the others. Nevertheless, the control system has been proven to be stable both in openloop and closed loop at Mach 0.75, Mach 1.5, and Mach 2.

The turbomachinery off-design behavior has been taken into account during the ascend trajectory up to Mach 3 and throttling. This has been possible thanks to the

introduction of the turbomachinery with performance maps and turbomachinery speed matching with respect to previous works. The fluid and spools inertia have been considered. This crucial aspect heavily influences the ATR overall performance, being the main cause for the differences noticed between steady-state and transient simulations.

Future works

While the produced model is capable of answering the research questions, the following enhancements could further increase the accuracy:

- A deeper study on the transient phenomena occurring withing the air intake,
- a better estimation of fluid and spool inertias,
- a more detailed study of the turbomachinery components, including the use of more representative maps and map scaling procedures,
- modelling the ATR integration into the full propulsion system, including DMR,
- implementation of more advanced controllers and tuning methods, able to account for non-linear behavior and cross-coupling.

Appendix A

Parallel Turbines

The Parallel turbines configuration has also been tested as alternative to the turbines in series. The work presented is in early stage of development and represent a starting point for further considerations. Nevertheless, some peculiarities can be already observed.

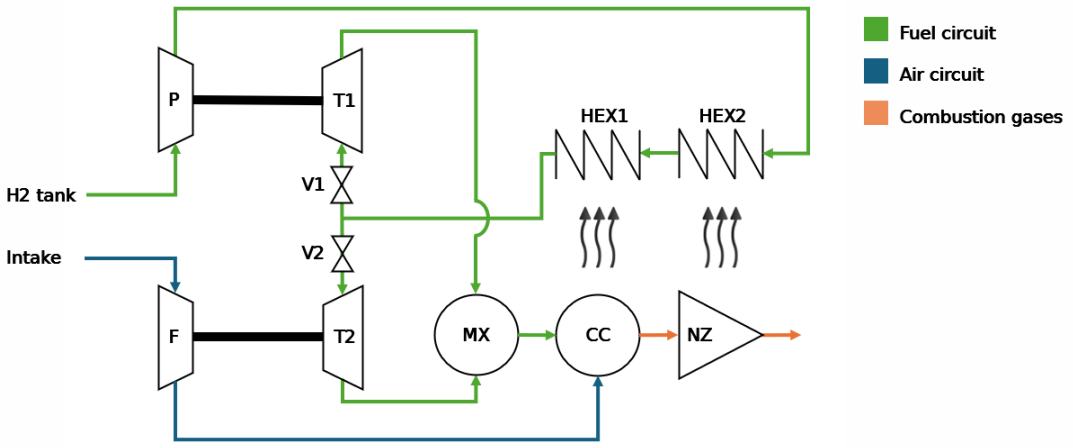

Figure A.1: Engine scheme with parallel turbines. In the mixer (MX), the two fuel flow rejoin.

The parallel turbines configuration has also been tested. The idea is to have the turbines arranged in parallel (A.1) with both branches experiencing the same pressure drop but different fuel flows, where the Pump Turbine receives a fraction of the total flow. For this to work without control, the expansion ratio scaling coefficient of the two turbines must be the same, while the mass flow scaling coefficient is calculated based on the requested power. Each branch is equipped

with a valve for control. Conceptually, maintaining a constant pressure drop in one branch while adjusting the valve in the other changes the turbine's operating point. However, within this model, this architecture has proven more challenging to control, resulting in poor performance in matching the references A.2.

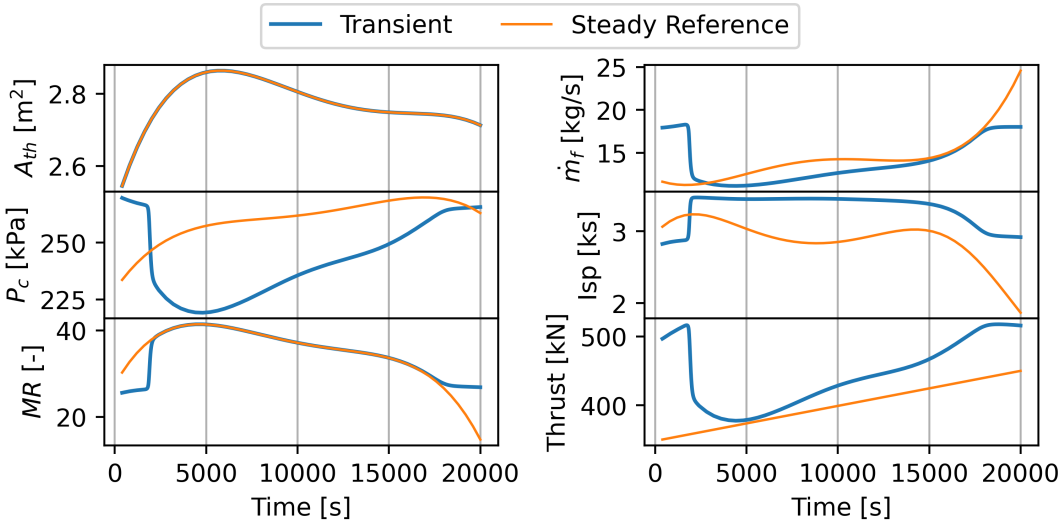

Figure A.2: Parallel turbines, throttle variables and $\dot{m}_f$, I_{sp}, thrust over time.

Comparing the throttle curve for the turbines in series versus those in parallel, the parallel configuration demonstrates significantly greater efficiency (see the specific impulse in A.2, generating more thrust even at a lower chamber pressure. Within this model, approximately a 10% difference in chamber pressure does not appear to affect thrust output significantly. The fuel flow is also reasonably matched. Despite the poor control, the parallel turbine configuration shows indications of better performance than the series arrangement.

The valve openings over time, illustrated in A.3, highlight the reasons behind the poor ability to match MR and P_c. To achieve the desired MR, the valve nearly closes completely. Even when the valve in series with the fan turbine opens fully, the resulting expansion ratio and mass flow are insufficient to provide adequate power to the fan. Improving the scaling of the fan map could position the operating points in a more efficient region of the map, thereby enhancing the system's ability to follow the set signals.

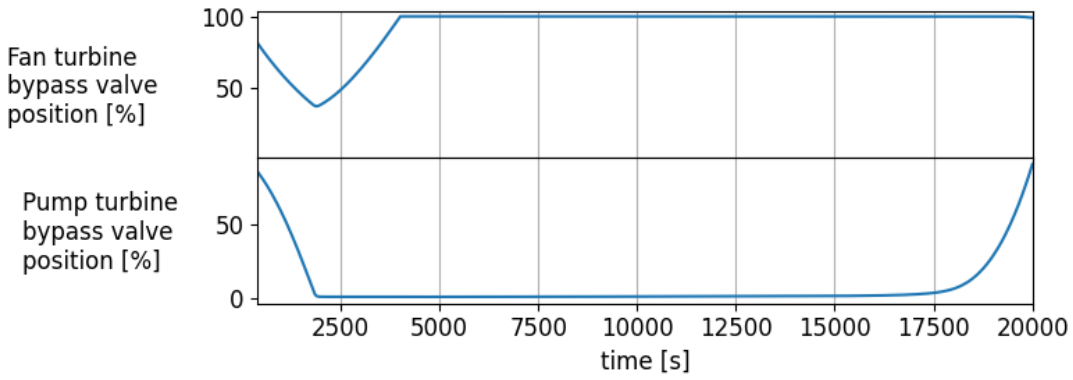

Figure A.3: Parallel turbines, valve position over time.

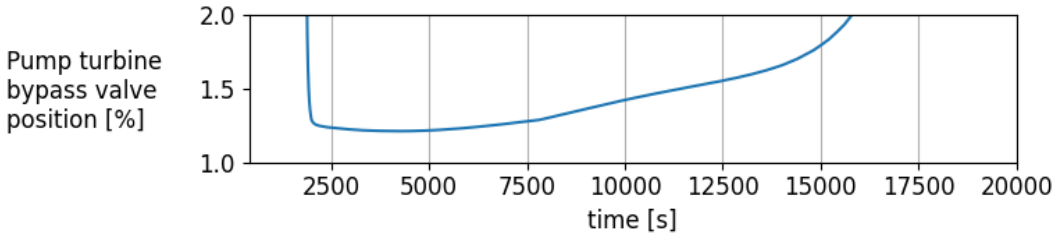

Figure A.4: Parallel turbines, zoom in of pump turbine valve opening over time.

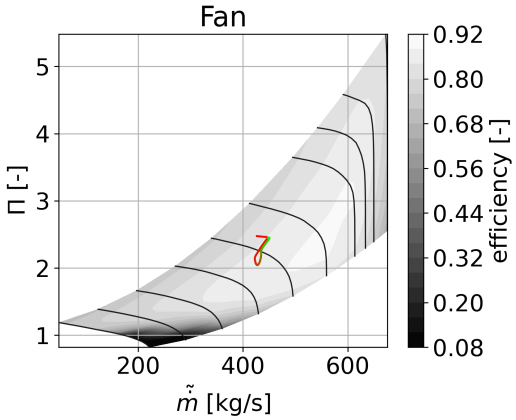

Figure A.5: Parallel turbines, locus of fan operating point. The color goes from red to green as time progresses

Figure A.5 shows how the operating points are within the map limits as in

previous cases with similar compression ratio and corrected mass flow rate. Even if

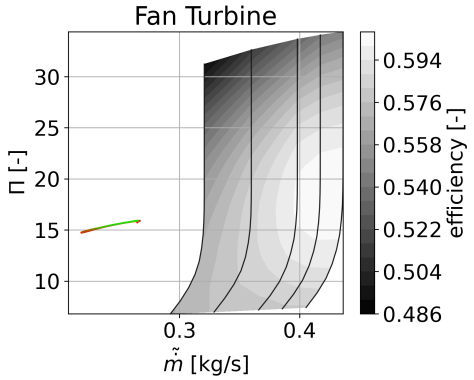

Figure A.6: Parallel turbines, locus of fan turbine operating point. The color goes from red to green as time progresses

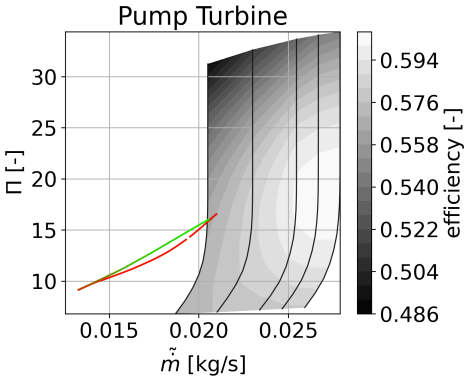

Figure A.7: Parallel turbines, locus of pump turbine operating point. The color goes from red to green as time progresses

the points are outside the map, the measured movements can be indication that a better scaling with the current procedure of turbines could be sufficient to model properly the turbines.

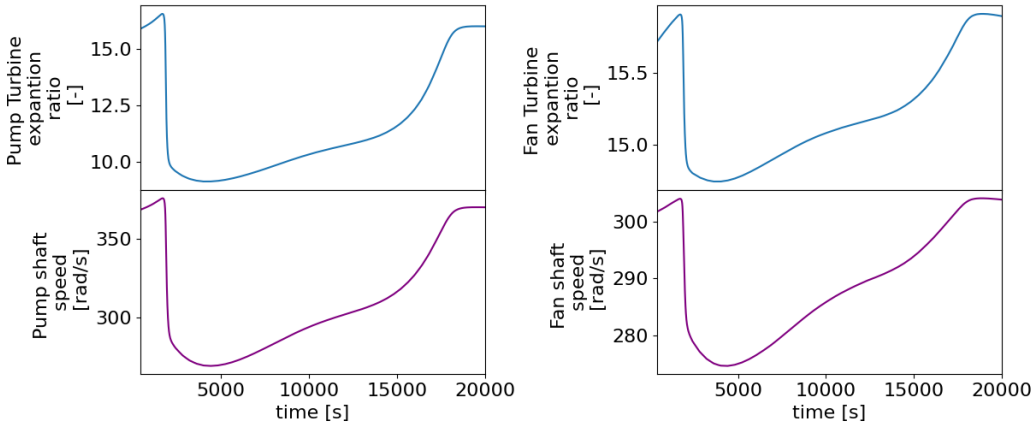

Figure A.8: Parallel turbines, shaft speed and turbines expansion ratio over time

As pictured in A.8 at lower MR the spools speed is higher. The parallel turbines configuration seems promising and viable alternative to the series one.

Bibliography

[1] N. Viola et al. «Main Challenges and Goals of the H2020 STRATOFLY Project». In: *Aerotecnica Missili & Spazio* 100.2 (June 2021), pp. 95–110. ISSN: 0365-7442, 2524-6968. DOI: 10.1007/s42496-021-00082-6. (Visited on 09/28/2023) (cit. on pp. vii, viii, 4, 5).

[2] S. Lighthill. *Boeing X-43*. https://www.dfrc.nasa.gov/Gallery/Photo/X-43A/HTML/ED98-44824-1.html. 1998 (cit. on pp. viii, 2).

[3] I R Miranda. *MODELING, ANALYSIS AND OPTIMIZATION OF THE AIR TURBO ROCKET EXPANDER ENGINE*. Project Report. June 2012 (cit. on pp. viii, 7).

[4] Kashkhan. *The Specific Impulse of Various Jet Engines (SSME Is the Space Shuttle Main Engine)*. https://en.wikipedia.org/wiki/Specific_impulse. Jan. 2009 (cit. on pp. viii, 8).

[5] KOJIMA T. and TANATSUGU N. «Development Study on Air Turbo-Ramjet for Space Plane». In: (2003) (cit. on pp. viii, 10).

[6] C Meerts and J Steelant. «Air Intake Design for the Acceleration Propulsion Unit of the LAPCAT-MR2 Hypersonic Aircraft». In: (2013) (cit. on pp. viii, 17).

[7] V. Fernández Villacé. «Simulation, Design and Analysis of Air-Breathing Combined-Cycle Engines for High Speed Propulsion». PhD thesis. Universidad Politécnica de Madrid, 2013. DOI: 10.20868/UPM.thesis.23340 (cit. on pp. viii, 18).

[8] S. L. Dixon and C. A. Hall. *Fluid Mechanics and Thermodynamics of Turbomachinery*. Seventh edition. Amsterdam ; Boston: Butterworth-Heinemann is an imprint of Elsevier, 2014. ISBN: 978-0-12-415954-9 (cit. on pp. viii, 19).

[9] GasTurb GmbH. *GasTurb 14*. 2021 (cit. on pp. viii, 22, 33).

[10] Wei G., Josage Chathura P., Daryl C., Sachin N., T. Wenning, K. Thirumaran, and E. Levine. «Variable-Speed Pump Efficiency Calculation For Fluid Flow Systems with and without Static Head». In: *InternatIonal Journal of energy ManageMent* 2.3 (2020) (cit. on pp. x, 64).

[11] D. R. Jenkins, T. Landis, and J. Miller. *American X-Vehicles: An Inventory X-1 to X-50 Centennial of Flight Edition*. NASA, June 2003 (cit. on p. 1).

[12] *MOREandLESS: Towards the Future of Civil Supersonic Aviation*. https://archivio-poliflash.polito.it/en/research_innovation/moreandless_towards_the_future_of_civil_supersonic_aviation. June 2021 (cit. on p. 4).

[13] J Steelant and T Langener. «THE LAPCAT-MR2 HYPERSONIC CRUISER CONCEPT». In: *29th Congress of the International Council of the Aeronautical Sciences*. Moscow, 2014 (cit. on p. 4).

[14] T Langener, S Erb, and J Steelant. «TRAJECTORY SIMULATION AND OPTIMIZATION OF THE LAPCAT-MR2 HYPERSONIC CRUISER CONCEPT». In: *29th Congress of the International Council of the Aeronautical Sciences*. St. Petersburg, Russia, July 2014 (cit. on p. 4).

[15] O. Gori, V. Borio, N. Viola, P. Roncioni, M. M., D. Pepelea, and M. G. Stoican. «From Conceptual to Preliminary Design: Aerodynamic Characterization of MR5 Civil High-Speed Aircraft». In: *25th AIAA International Space Planes and Hypersonic Systems and Technologies Conference*. Bengaluru, Karnataka, India: American Institute of Aeronautics and Astronautics, May 2023. ISBN: 978-1-62410-710-8. DOI: 10.2514/6.2023-3005. (Visited on 09/30/2023) (cit. on p. 4).

[16] I. Rodríguez-Miranda, V. Fernández-Villacé, and G. Paniagua. «Modelling, Analysis, and Optimization of the Air-Turborocket Expander Engine». In: *Journal of Propulsion and Power* 29.6 (Nov. 2013), pp. 1266–1273. ISSN: 0748-4658, 1533-3876. DOI: 10.2514/1.B34781. (Visited on 03/13/2023) (cit. on pp. 5, 36).

[17] G. P. Sutton and O. Biblarz. *Rocket Propulsion Elements* (cit. on p. 8).

[18] William H. Heiser and David T. Pratt. *Hypersonic Airbreathing Propulsion*. AIAA Education Series. Washington, D.C: American Institute of Aeronautics and Astronautics, 1994. ISBN: 978-1-56347-035-6 (cit. on p. 9).

[19] V. Balepin. «High Speed Propulsion Cycles». In: *Advances on Propulsion Technology for High-Speed Aircraft* (2008) (cit. on p. 9).

[20] C Segal. «PROPULSION SYSTEMS FOR HYPERSONIC FLIGHT». In: *RTO-EN-AVT-116* () (cit. on p. 9).

[21] F Jivraj, R Varvill, A Bond, and G Paniagua. «The Scimitar Precooled Mach 5 Engine». In: (2007) (cit. on p. 9).

[22] M Thomas and A Leonard. «Air-Turbo-Rocket Combustion». In: *33rd Aerospace Sciences Meeting and Exhibit*. Reno,NV,U.S.A.: American Institute of Aeronautics and Astronautics, Jan. 1995. DOI: 10.2514/6.1995-813. (Visited on 07/09/2024) (cit. on p. 9).

[23] V. Fernández-Villacé, G. Paniagua, and J. Steelant. «Installed Performance Evaluation of an Air Turbo-Rocket Expander Engine». In: *Aerospace Science and Technology* 35 (May 2014), pp. 63–79. ISSN: 12709638. DOI: 10.1016/j.ast.2014.03.005. (Visited on 07/10/2024) (cit. on p. 9).

[24] T. Sato, H. Taguchi, H. Kobayashi, T. Kojima, K. Fukiba, D. M. Okai K., K. Fujita, M. Hongo, and S. Sawai. «Development Study of a Precooled Turbojet Engine». In: *Acta Astronautica* 66.7-8 (Apr. 2010), pp. 1169–1176. ISSN: 00945765. DOI: 10.1016/j.actaastro.2009.10.006. (Visited on 07/10/2024) (cit. on p. 10).

[25] V. Fernández-Villacé, G. Paniagua, and J. Steelant. «Installed Performance Evaluation of an Air Turbo-Rocket Expander Engine». In: *Aerospace Science and Technology* 35 (May 2014), pp. 63–79. ISSN: 12709638. DOI: 10.1016/j.ast.2014.03.005. (Visited on 03/15/2023) (cit. on p. 12).

[26] Pedro M. Goncalves, Ali C. Ispir, and Bayindir H. Saracoglu. «Development and Optimization of a Hypersonic Civil Aircraft Propulsion Plant with Regenerator System». In: *AIAA Propulsion and Energy 2019 Forum*. Indianapolis, IN: American Institute of Aeronautics and Astronautics, Aug. 2019. ISBN: 978-1-62410-590-6. DOI: 10.2514/6.2019-4421. (Visited on 03/15/2023) (cit. on p. 12).

[27] A. C. Ispir, B. O. Cakir, and B. H Saracoglu. «Design Space Exploration for a Scramjet Engine by Using Data Mining and Low-Fidelity Design Techniques». In: *2nd International Conference on High-Speed Vehicle Science & Technology*. Bruges, Belgium: Council of European Aerospace Societies, 2022 (cit. on p. 12).

[28] Emoresarios Agrupados. *EcosimPro User Manual*. 2013 (cit. on p. 14).

[29] L. Petzhold. «A Description of DASSL: A Differential/Algebraic System Solver». In: *Proc. 10th IMACS World Congress*. 1982 (cit. on p. 14).

[30] ESA,Emoresarios Agrupados. *ESPSS 3.6.0 User Manual*. 2022 (cit. on pp. 15, 23).

[31] C Meerts, J Steelant, and P Hendrick. *PRELIMINARY DESIGN OF THE LOW SPEED PROPULSION AIR INTAKE OF THE LAPCAT-MR2 AIRCRAFT* (cit. on p. 17).

[32] V. Fernández Villacé. «Simulation, Design and Analysis of Air-Breathing Combined-Cycle Engines for High Speed Propulsion». PhD thesis. Universidad Politécnica de Madrid, 2013. DOI: 10.20868/UPM.thesis.23340. (Visited on 07/05/2024) (cit. on p. 18).

[33] J. Kurzke and I. Halliwell. *Propulsion and Power*. Cham: Springer International Publishing, 2018. ISBN: 978-3-319-75977-7 978-3-319-75979-1. DOI: 10.1007/978-3-319-75979-1. (Visited on 08/30/2024) (cit. on p. 21).

[34] Sanford G. and B. J McBride. *Computer Program for Calculation of Complex Chemical Equilibrium Compositions and Applications*. Tech. rep. Reference publication 1311. National Aeronautics and Space Administration, Oct. 1994 (cit. on p. 23).

[35] D.R. Bartz. «Turbulent Boundary-Layer Heat Transfer from Rapidly Accelerating Flow of Rocket Combustion Gases and of Heated Air11This Chapter is contributed jointly by the author and the Jet Propulsion Laboratory, California Institute of Technology, where portions of the work were done under Department of the Army Contract No. DA-04-495-Ord 18 and National Aeronautics and Space Administration Contract Nos. NASw-6 and NAS 7-100.» In: ed. by J. P. Hartnett and T. F. Irvine. Vol. 2. Advances in Heat Transfer. Elsevier, 1965, pp. 1–108. DOI: https://doi.org/10.1016/S0065-2717(08)70261-2. URL: https://www.sciencedirect.com/science/article/pii/S0065271708702612 (cit. on p. 27).

[36] P.G. Hill and C.R. Peterson. «Mechanics and Thermodynamics of Propulsion». In: Addison-Wesley, 1992, p. 546. ISBN: 978-0-201-14659-2 (cit. on p. 28).

[37] B. Fraeijs de Veubeke M. Barrére A. Jaumotte and J. Vandenkerckhove. «Rocket Propulsion». In: Elsevier Publishing Company, 1960, p. 115 (cit. on p. 28).

[38] Yunus A. Çengel and Afshin J. Ghajar. *Heat and Mass Transfer: Fundamentals & Applications*. 5th edition. New York, NY: McGraw-Hill Education, 2015, p. 496. ISBN: 978-0-07-339818-1 (cit. on p. 29).

[39] *Manual of the ICAO Standard Atmosphere - Extended to 80 Kilometres / 262,500 Feet*. 3rd Edition. 1993 (cit. on p. 31).

[40] E.W. Lemmon, M.O. McLinden, and M.L. Huber. *NIST Standard Reference Database23: Reference Fluid Thermodynamic and Transport Properties - REFPROP, Version 7.0. National Institute of Standards and Technology, Standard Reference Data Program.* 2002 (cit. on p. 32).

[41] «Centrifugal Compressors During Fast Transients». In: *Journal of Engineering for Gas Turbines and Power* (2011) (cit. on p. 33).

[42] T. Verstraete. «CADO: A Computer Aided Design and Optimization Tool for Turbomachinery Applications». In: *2nd International Conference on Engineering Optimization*. Lisbon, Portugal, 2010 (cit. on p. 35).

[43] W. Lanz. «Module 3: Hydrogen Use in Internal Combustion Engines». In: *Hydrogen Fuel* (2001) (cit. on p. 53).